Fakultät für Physik und Astronomie
Ruprecht-Karls-Universität Heidelberg

Diplomarbeit
Im Studiengang Physik

vorgelegt von

Martin Höcker

aus Clausthal-Zellerfeld

2010

Untersuchungen zum Ionentransfer im UW/MPIK Doppel-Penningfallen Experiment

Die Diplomarbeit wurde von Martin Höcker
ausgeführt am
Max-Planck-Insitut für Kernphysik
unter der Betreuung von
Herrn Prof. Dr. Klaus Blaum

sowie von

Herrn Priv.-Doz. Dr. José Ramon Crespo López-Urrutia
Max-Planck-Institut für Kernphysik Heidelberg

Department of Physics and Astronomy
University of Heidelberg

Diploma Thesis
in Physics

submitted by
Martin Höcker

born in Clausthal-Zellerfeld
2010

Ion Transfer Studies in the UW/MPIK Double-Penning Trap Experiment

This diploma thesis has been carried out by Martin Höcker
at the
Max-Planck-Institute for Nuclear Physics
under the supervision of
Prof. Klaus Blaum

and

Priv.-Doz. Dr. José Ramon Crespo López-Urrutia
Max-Planck-Institute for Nuclear Physics, Heidelberg

Untersuchungen zum Ionentransfer im UW/MPIK Doppel-Penningfallen Experiment

Das UW/MPIK-PTMS Experiment ist ein neues Penning-Fallen Massenspektrometer, welches an der University of Washington in Seattle entwickelt wurde, um das Massenverhältnis von ^{3}H und ^{3}He mit einer relativen Unsicherheit von weniger als 10^{-11} zu bestimmen. Um diese Genauigkeit zu erreichen, wird ein sogenanntes Doppelfallen-System, bestehend aus einer Präparations- und einer Messfalle, eingesetzt. Dieses ermöglich einen schnellen Austausch der Ionen, an denen die Messungen durchgeführt werden.

Im Jahre 2008 wurde das Experiment nach Aufbau eines speziell dafür vorbereiteten Labors nach Heidelberg umgezogen, erweitert und im Rahmen dieser Arbeit neu aufgebaut. Erste Experimente zur Charakterisierung dieses Präzisionsmassenspektrometers zielten auf die interne und externe Ionenerzeugung ab sowie auf die Ausrichtung des Fallenturms in Bezug auf die Magnetfeldorientierung, den effizienten Ionentransport und den ersten Nachweis gespeicherter Ionen in beiden Penningfallen.

Ion Transfer Studies in the UW/MPIK Double-Penning Trap Experiment

The UW/MPIK-PTMS experiment is a new Penning trap mass spectrometer that was designed at the University of Washington, Seattle, for a determination of the ^{3}H/^{3}He mass ratio with a relative uncertainty of less than 10^{-11}. In order to reach this precision, it features a double-trap setup consisting of a preparation trap and a measurement trap, which allows fast swichting of the investigated ions.

In the year 2008 the experiment was moved to Heidelberg, where a new lab had been set up to meet its specific requirements. In the scope of this thesis the experiment was set up and some systems were upgraded. The calculations and first commissioning experiments described here aimed at the characterization of internal and external ion creation, the alignment of the trap tower relative to the magnetic field orientation, effective ion transport procedures, and the first detection of stored ions in both Penning traps.

Erklärung:

Ich versichere, dass ich diese Arbeit selbständig verfasst habe und keine anderen als die angegebenen Quellen und Hilfsmittel benutzt habe.

Heidelberg, den 17.02.2009 .....

Contents

Chapter 1

Introduction

Penning traps are tools for storing charged particles within electric and magnetic fields, and can be used to study the properties of those particles, such as their magnetic moment or mass. The UW/MPIK PTMS is a new Penning trap experiment that was specifically designed to measure the mass ratio of the hydrogen isotope ^{3}H and the helium isotope ^{3}He, which is an important parameter in the ongoing search of the electron-antineutrino mass.

The main focus of this thesis is on examining a specific component of our experiment: The ion transport between an external ion source and two Penning traps. While the implementation of these transports is not vitally important at this stage of the experiment, concentrating on them allows me to describe the most important parts of the setup, and in particular some systems that have not yet been described in detail in previous publications. It also allows me to present a subset of the commissioning experiments that have been performed in the last year.

In the following sections of this chapter I will give a short introduction to Penning trap mass spectrometry in general, and our spectrometer in particular. Section 1.3 contains a brief motivation of the significance of the ^{3}H-^{3}He mass-difference measurements.

The theory behind Penning trap mass spectrometry and behind ion transport in strong magnetic fields is outlined in chapter 2. Chapter 3 and chapter 4 detail the experimental setup, with the latter introducing the ion transfer schemes. The results of the commissioning experiments are reported in chapter 5. They are used in chapter 6

to discuss the feasibility of the most challenging ion transport scheme. An outlook to the next steps of the experiment is given in chapter 7.

1.1 Penning Trap Mass Spectrometry

In the last 30 years [1], Penning traps have become the most accurate tool to measure nuclear masses. A relative uncertainty on the level of 10^{-8} has been reached for unstable isotopes with half- lives of less than 100 ms [2], and the masses of stable nuclei can be measured with a uncertainty of 10^{-11} and below [3]. This high accuracy is achieved by measuring the cyclotron frequencies for different species of ions in the same magnetic field. Since frequencies can be measured very accurately, the measurement uncertainty for stable nuclei is mainly limited by fluctuations of the magnetic and electric fields between the measurements. This can be mitigated by either measuring the two ion species simultaneously, or by decreasing the time between measurements. The former technique was developed and demonstrated by the group of D. Pritchard [4], but their method requires the two ions to have a relative mass difference between 10^{-3} and 10^{-4}.

Because the ion species we are interested in, namely ^{3}H and ^{3}He, have a mass difference of less than 10^{-5}, our technique to decrease the measurement uncertainty focuses on decreasing the dead-time between the measurements, and on the best possible control of environmental paramters that influence the measurement precision.

1.2 The UW/MPIK PTMS

The **U**niversity of **W**ashington/**M**ax-**P**lanck-**I**nstitut für **K**ernphysik **P**enning **T**rap **M**ass **S**pectrometer was designed to perform non-destructive measurements of the masses of single ions. This single-ion technique reduces systematic effects that can arise with higher ion numbers, but the preparation of the Penning trap with a single ion often requires hours of work, since after each loading all unwanted ions must be removed from the trap. Three requirements drove the development of the UW/MPIK PTMS:

1. decreasing the time between measurements,

2. decreasing the noise of the electric and magnetic fields that are used, and

3. minimizing contamination of the traps with the radioactive ^{3}H.

To satisfy the first requirement, a double-trap design was chosen: While one trap is used for high-precision measurements on one of the single ions, the second trap stores the other single ion. An ambitious scheme was developed to switch these ions, which reduces the time between precision measurements from hours to minutes.

The second requirement was accomplished by installing systems that compensate many of the external fluctuations, for example: room temperature stabilization, magnet cryostat pressure control, and magnetic field fluctuation compensation.

The final requirement was realized with an external ion source: In previous experiments [5] the traps were loaded by introducing small quantities of neutral gas into the traps, and then ionizing this gas with an electron beam. Because eventually most of the gas that is flowed into the traps will adhere to the trap walls, contamination with radioactivity becomes an issue. The emitted β-electrons can load the traps unintenionally with contaminant ions through rest gas ionization, which decreases the measurement precision. The external ion source, on the other hand, provides a low-intensity beam of ions that can be switched on and off quickly, which reduces the total amount of tritium that is transported into the traps.

1.3 The ^{3}H-^{3}He Mass Difference and the Mass of the Neutrino

In the Standard Model of particle physics, the neutrino mass m_ν is assumed to be zero. However, recent observations in cosmology [6] and the discovery of oscillations between the neutrino flavors [7] point towards a neutrino mass in the order of 1 eV. Since neutrinos interact only weakly with matter, their masses are not accessible through direct measurements. One indirect method for obtaining information about the absolute mass of the electron-antineutrino uses characteristics of the tritium β-decay. Tritium is a radioactive isotope of hydrogen and decays to the helium isotope ^{3}He:

$$^3\mathrm{H} \longrightarrow ^3\mathrm{He} + \mathrm{e}^- + \bar{\nu}_e + E_0 + E_f \quad . \tag{1.1}$$

The total energy released in this decay is given by $E_0 + E_f$. The term E_f denotes the energy of the final state of the mother atom (including the recoil energy) and is of the order of 20 eV. The energy E_0, which amounts to approximately 18.6 keV, designates the kinetic energy that is distributed between the electron and the antineutrino. Since historically the neutrino was thought to be massless, E_0 also includes the rest mass of the antineutrino.

So far, E_0 has not been measured directly, since the energy of the antineutrino cannot be observed with the tools that are available today. But by taking an energy spectrum of the β-electrons of many tritium decays, E_0 can be identified with the endpoint of this spectrum (see figure 1.1). A decay near this endpoint corresponds to a case, where the majority of the kinetic energy is carried away by the electron, and the antineutrino is essentially at rest. Depending on the mass of the antineutrino, the shape of the spectrum near the endpoint deviates from the clasically expected spectrum, where the m_ν assumed to be zero. In principle, this deviation can be used to obtain the neutrino mass as a parameter of a fit function, but measurements that were carried out with this technique have so far only placed upper limits on the neutrino mass. The most accurate experiment of this type, the Mainz Neutrino Mass Experiment, has given an upper limit of $m_\nu \leq 2.3\,\mathrm{eV}/c^2$ (95% C.L.) [8] .

A new experiment to measure the spectrum near the endpoint energy is being commissioned at the Karlsruhe Insititute of Technology [9]. If no finite m_ν is found, it aims to reduce the upper limit on the neutrino mass to $0.2\,\mathrm{eV}/c^2$. Because the total energy release E_0 is one of the fit parameters of the spectrum, an independent measurement of the ^{3}H-^{3}He mass difference with a uncertainty of less than 0.2 eV is needed to check systematic uncertainties of this new β-spectrometer experiment. Presently, the most precise value for this mass difference is $(18,589.8 \pm 1.2)\,\mathrm{eV}/c^2$ [10]. Our goal is to reduce the uncertainty of this value by at least one order of magnitude, which requires a mass ratio measurement of ^{3}H and ^{3}He with a relative uncertainty on the level of 10^{-11}.

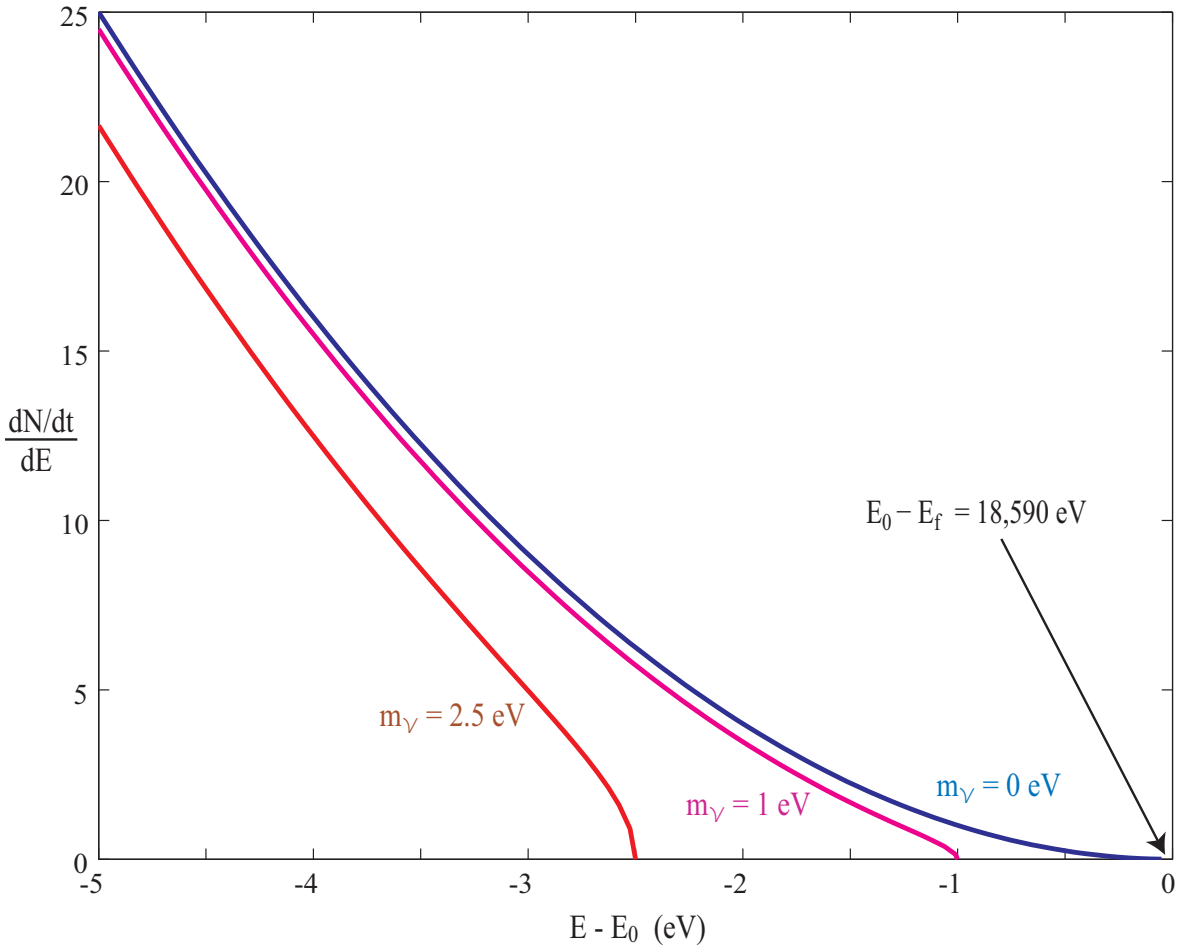

Figure 1.1: Expected spectrum of the tritium beta decay for different possible values of the neutrino mass. A finite neutrino mass changes the shape of the spectrum in a characteristic way that is especially pronounced near the endpoint E_0. The neutrino mass m_ν can be obtained by fitting a model with the parameters E_0 and m_ν to an experimentally taken spectrum. An independent measurement of the total energy release $E_0 + E_f$ via the ^{3}H-^{3}He mass-difference can be used to check for systematic errors in the spectrum.

Chapter 2

Theory

A Penning trap uses static electric and magnetic fields to confine charged particles. It is named after Frans Michel Penning, who utilized an axial magnetic field for radial confinement of electrons in a low pressure vacuum gauge [11]. In the 1940's, J.R. Pierce used the same principle of radial confinement with a magnetic field, and added two electrodes, the "end caps", for axial confinement to build a 3-dimensional trap [12]. In the 1960's and 1970's the group of H. Dehmelt at the University of Washington turned this type of trap into a tool for storing and detecting *single* electrons and ions. This allowed them to conduct measurements of the electron g-factor [13] and ion masses [14] with a precision of 10^{-9} and better. A more detailed overview of the history and current developments in mass spectrometry can be found in [1].

In this chapter I will give a short introduction to the theory behind our externally loaded double Penning trap, focusing on areas that are relevant to the ion transport between the ion source and traps. Of special interest are radii of the periodic ion motion, which limit the localization of the ion at the beginning of a transport sequence. These radii can be estimated using an energy–radius relationship (section 2.1.2), the sideband cooling limits (section 2.1.3), and adiabatic invariants (section 2.2.1). The ion transport itself can be treated in a simplified way using a guiding center motion (section 2.2.2).

2.1 Principle of the Penning Trap

2.1.1 Electric and Magnetic Fields

A charged particle moving perpendicular to a homogeneous magnetic field is deflected by the Lorentz force $\vec{F_l} = q\vec{v} \times \vec{B}$ onto a circular orbit. The frequency of this motion, called the cyclotron frequency ν_c, depends (for non-relativistic energies) only on the strength of the magnetic field and the particle's charge-to-mass ratio:

$$\nu_c = \frac{\omega_c}{2\pi} = \frac{1}{2\pi}\frac{|q|}{m}B \quad . \tag{2.1}$$

The mass ratio of two ions can therefore be obtained by comparing their cyclotron frequencies in the same magnetic field. However, a homogeneous magnetic field only confines charged particles radially. For axial confinement, a Penning trap uses an electric quadrupole field. If we define the direction of the magnetic field as the z-direction, the electrostatic potential of an ideal Penning trap can be written as:

$$\Phi(x, y, z) = \frac{V_R}{2d^2}\left(z^2 - \frac{1}{2}\left(x^2 + y^2\right)\right) = \frac{V_R}{2d^2}\left(z^2 - \frac{1}{2}\rho^2\right) \quad , \tag{2.2}$$

with the voltage V_R being proportional to the axial well depth. The minus sign ensures that Φ satisfies the Laplace equation. The definition of d, which is proportional to the trap size, depends on the trap geometry. An ideal quadrupolar field can be created with electrodes that are hyperboloids of revolution (see figure 2.1). Their shape is given by the implicit equation

$$z^2 - \frac{1}{2}\rho^2 = {z_0}^2 \tag{2.3}$$

for the endcaps, and

$$z^2 - \frac{1}{2}\rho^2 = -{\rho_0}^2 \tag{2.4}$$

for the ring electrode. The parameters ρ_0 and z_0 are the minimum distances from the electrodes to the trap center. If we now define

$$d^2 = \frac{1}{2}({z_0}^2 + \frac{1}{2}{\rho_0}^2) \quad , \tag{2.5}$$

then V_R can be identified with the electric potential between ring electrode and endcaps. In our setup the endcaps are held near ground and the ring electrode is biased with a negative voltage V_0. This is equivalent to adding a constant to (2.2). The ring voltage is then simply given as $V_0 = -V_R$.

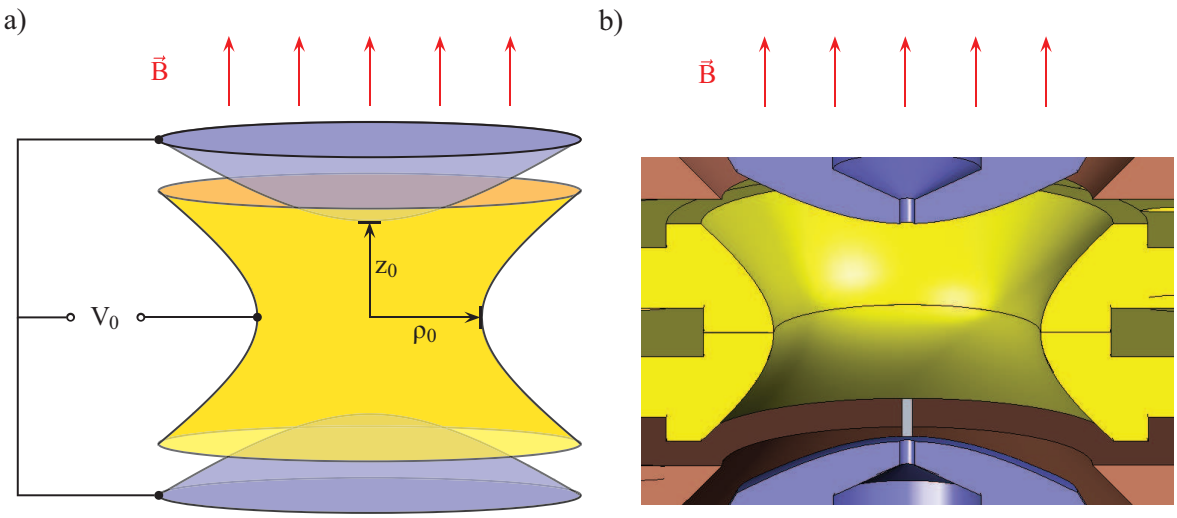

Figure 2.1: The left hand side shows a model of a simple Penning trap. The ring electrode is shown in yellow, the endcaps in blue. The right hand side shows a cutaway view of a realistic trap, where the endcaps have central holes for ion transfers. The guard-electrodes, shown in brown, can be used to compensate low order field inhomogeneities, and to couple radio frequency (RF) signals into the trap.

2.1.2 Equations of Motion

Using Newton's second law and the Lorentz force equation, we can state the equations of motion:

$$\ddot{\vec{r}} = \frac{q}{m}\left(\vec{E} + \dot{\vec{r}} \times \vec{B}\right) \quad . \tag{2.6}$$

Substituting $\vec{E} = -\vec{\nabla}\Phi$ and $\vec{B} = B\vec{e}_z$, (2.6) can be written as:

$$\ddot{x} = \frac{q}{m}\left(\frac{V_R}{2d^2}x + B\dot{y}\right) \tag{2.7}$$

$$\ddot{y} = \frac{q}{m}\left(\frac{V_R}{2d^2}y - B\dot{x}\right) \tag{2.8}$$

$$\ddot{z} = -\frac{qV_R}{md^2}z \quad . \tag{2.9}$$

The solution for (2.9) is a simple harmonic motion:

$$z\,(t) = \rho_z \sin(\omega_z t + \phi_z) \quad . \tag{2.10}$$

The axial frequency is given by

$$\nu_z = \frac{\omega_z}{2\pi} = \frac{1}{2\pi}\sqrt{\frac{qV_R}{md^2}} \quad , \tag{2.11}$$

while the amplitude ρ_z and phase ϕ_z depend on initial conditions. The coupled differential equations (2.7) and (2.8) can be solved by decoupling them with the substitution $\alpha = x + iy$. Assuming a positive charge q, the substitution yields

$$\ddot{\alpha} + \mathrm{i}\omega_c\dot{\alpha} - \frac{1}{2}\omega_z^2\alpha = 0 \quad . \tag{2.12}$$

The ansatz $\alpha = \exp(-\mathrm{i}\omega t)$ leads to the characteristic polynomial

$$\omega^2 - \omega_c\omega + \frac{1}{2}\omega_z^2 = 0 \quad . \tag{2.13}$$

The solutions of this equation are the eigenfrequencies

$$\omega_\pm = \frac{1}{2}\left(\omega_c \pm \sqrt{\omega_c^2 - 2\omega_z^2}\right) \equiv 2\pi\nu_\pm \quad . \tag{2.14}$$

The frequency ν_+ is called reduced cyclotron frequency, since it is typically close to the free space cyclotron frequency ν_c. The second frequency, ν_-, is referred to as the magnetron frequency. The general solution of (2.12) is a superposition of the two fundamental solutions.

$$\alpha = \alpha_+ \exp(-\mathrm{i}\omega_+ t) + \alpha_- \exp(-\mathrm{i}\omega_- t) \tag{2.15}$$

By comparing the imaginary and real parts of (2.15) with the substitution $\alpha = x + \mathrm{i}y$, we can state the general solution of the radial equations of motion. Together with the axial motion (2.10), the ion trajectory inside a Penning trap can be written as:

$$x(t) = +\rho_+ \cos(\omega_+ t + \phi_+) + \rho_- \cos(\omega_- t + \phi_-) \quad , \tag{2.16}$$

$$y(t) = -\rho_+ \sin(\omega_+ t + \phi_+) - \rho_- \sin(\omega_- t + \phi_-) \quad , \tag{2.17}$$

$$z(t) = \rho_z \sin(\omega_z t + \phi_z) \quad . \tag{2.18}$$

For negative ions, the signs on the right hand side of equation (2.17) would be positive. The phases ϕ_i and radii ρ_i depend on initial conditions. This trajectory is a superposition of three periodic motions: A linear oscillation in the axial direction and two circular motions in the radial plane. The faster of the two circular motions is often called cyclotron motion, since it's frequency and radius are comparable to a free space cyclotron motion. The slower circular motion is referred to as magnetron motion, which can be thought of as an $\vec{E} \times \vec{B}$ drift around the trap center. An example of such

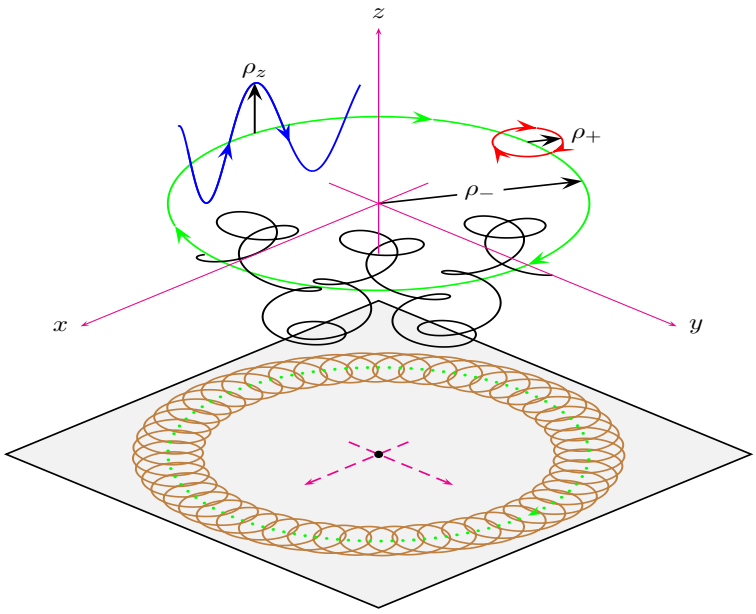

Figure 2.2: Ion trajectory in a Penning trap. The trajectory is a superposition of three separate motions: An axial oscillation with a frequency of ν_z (shown in blue), a slow radial circulation around the trap center with ν_- (magnetron motion, green) and a fast circulation with ν_+ (cyclotron motion, red). The superposition is illustrated in black, while the brown curve on the bottom shows a two-dimensional projection onto the x-y-plane.

an ion trajectory is shown in figure 2.2, while approximate frequencies of ions in our trap are summarized in table 2.1.

By examining the total energy of the particle, we can derive a relationship between the motional radii and the energy in each mode. The total energy is given by the sum of the kinetic and potential energy:

$$E = \frac{1}{2}m\dot{\vec{r}}^2 + q\Phi(\vec{r}) \tag{2.19}$$

$$= \underbrace{\frac{1}{2}m\omega_z^2\rho_z^2}_{E_z} + \underbrace{\frac{1}{2}m\rho_+^2\omega_+\left(\omega_+ - \omega_-\right)}_{E_+} + \underbrace{\frac{1}{2}m\rho_-^2\omega_-\left(\omega_- - \omega_+\right)}_{E_-} \quad . \tag{2.20}$$

Note that the magnetron motion gives a negative contribution to the total energy of the particle, as it must, since the radial electric field pulls the ion outwards. Removing energy from the magnetron mode (through damping forces, for instance) will increase the magnetron radius until the particle hits an electrode. Fortunately, it can be shown [15] that the magnetron motion has such a large damping time, that it can be seen as stable for all practical purposes.

Table 2.1: Calculated frequencies of protons and singly charged ^{3}H/^{3}He ions in our trap (B = 5.3 T and d = 2.11 mm). For precision measurements, the ring voltage V_0 is chosen such, that the axial frequency is locked to 4 MHz. A ring voltage of -0.5 V is relevant for ion transfers.

	$m = 1$ u		$m = 3$ u	
	V_0 = -29.4 V	V_0 = -0.5 V	V_0 = -87.8 V	V_0 = -0.5 V
ν_z	4.0 MHz	521.9 kHz	4.0 MHz	301.1 kHz
ν_+	80.7 MHz	80.8 MHz	26.7 MHz	27.0 MHz
ν_-	99 kHz	1.7 kHz	299 kHz	1.7 kHz
ν_c	80.8 MHz	80.8 MHz	27.0 MHz	27.0 MHz

In a perfect trap, the relation $\omega_c = \omega_+ + \omega_-$ gives the free space cyclotron frequency. In a real trap, however, the magnetic and electric fields deviate from their ideal configuration. The electrostatic perturbations can be partly compensated by so-called "guard electrodes" (see figure 2.1) between the endcaps and the ring, but because of, e.g., patch potentials on the electrode surfaces [16] and machining limitations, a certain level of perturbation will always be present [17]. The magnetic field perturbations are, in a well shimmed magnet, dominated by the paramagnetic materials of the trap [18]. A third imperfection is the error of alignment between the magnetic and electric field axes. Fortunately, it can be shown that the sum

$$\omega_c^2 = \omega_+^2 + \omega_-^2 + \omega_z^2 \tag{2.21}$$

holds true for all low order perturbations of the electric field, and for a misalignmet of the magnetic field [19]. This relation, called the "Invariance Theorem", is the reason for the high level of precision that is possible with Penning trap mass spectrometry [20].

In a non-ideal Penning trap, the axial frequency also depends slightly on the energies E_- and E_+ of the magnetron and cyclotron mode [15]. This can be used to detect ω_- and ω_+ indirectly, by monitoring the axial frequency while exciting the magnetron and cyclotron mode with dipole RF signals at ν_- and ν_+.

2.1.3 Energy of the Cooled Ion

The periodic movement of the single ion induces tiny image currents in the trap electrodes. Since the electrodes have finite resistance, the image current dissipates some of the ion's energy, until it is in thermal equilibrium with the electrodes. In our case, this effect is very small for the magnetron and cyclotron mode; their damping times τ_+ and τ_- are of the order of hundreds of years [19] and therefore much longer than typical measurement times. The axial damping time τ_z is between 0.2 s and 2 s, because we use the image current of the axial motion to detect the ion with a resonant LC circuit. In order to cool the ion and to increase the signal-to-noise ratio, the trap and the first amplifier stages of the detection circuit are submerged in liquid helium (see chapter 3.1). However, since the detection circuit couples some electrical noise onto the endcaps, the axial motion thermalizes to a temperature that is slightly higher than the 4-K liquid helium bath. Similar setups have estimated this temperature to be around 10 K [21].

Using the "guard electrodes" (see figure 2.1), dipolar and quadrupolar radio frequency (RF) fields can be coupled into the trap to manipulate the ion motion. Dipole fields can be used to excite one of the ion's normal modes (axial, magnetron or cyclotron motion), while quadrupolar fields can be used to transfer energy from one mode to another [22]. Since the axial mode quickly thermalizes to the trap temperature, the magnetron and cyclotron mode can be cooled by coupling them to the axial mode. The minimum energies in those modes that are possible with this technique are given by the cooling limit [15]:

$$E_- = \frac{\omega_m}{\omega_z} E_z \tag{2.22}$$

$$E_+ = \frac{\omega_c}{\omega_z} E_z \tag{2.23}$$

where E_z is the axial energy given by $E = kT_z$ with T_z at approximately 10 K. The cooling limit and equation (2.20) allow us to estimate the radii of each mode, which are summarized in table 2.2.

Table 2.2: Calculated energies and motion radii for protons and singly charged ^{3}H/^{3}He ions in the cooling limit. Parameters used were $B = 5.3\,\mathrm{T}$, $E_z = 10\,\mathrm{K}\ k_B$ and $V_0 = -29.4\,\mathrm{V}$ for protons, $V_0 = -87.8\,\mathrm{V}$ for ^{3}H/^{3}He ions. The motion radii scale with the square root of the axial energy. Note: In the cooling limit the magnetron radius ρ_- and the cyclotron radius ρ_+ are exactly the same.

	E_z	ρ_z	E_+	ρ_+	E_-	ρ_-
$m = 1\,\mathrm{u}$	$8.8 \times 10^{-4}\,\mathrm{eV}$	$16.1\,\mu\mathrm{m}$	$1.8 \times 10^{-2}\,\mathrm{eV}$	$6.3\,\mu\mathrm{m}$	$2.1 \times 10^{-5}\,\mathrm{eV}$	$6.3\,\mu\mathrm{m}$
$m = 3\,\mathrm{u}$	$3.8 \times 10^{-4}\,\mathrm{eV}$	$9.3\,\mu\mathrm{m}$	$5.8 \times 10^{-3}\,\mathrm{eV}$	$3.6\,\mu\mathrm{m}$	$6.5 \times 10^{-7}\,\mathrm{eV}$	$3.6\,\mu\mathrm{m}$

2.2 Ion Transport in a Magnetic Field

The calculation of ion dynamics in a magnetic field can be greatly simplified by choosing the appropriate mathematical tools. In a strong magnetic field, for instance, the ions are radially confined around the field lines. So if we are only interested in axial movement in strong fields, it may be enough to take a one-dimensional approach. This can be justified in a more stringent way by applying the principle of the "guiding center motion", which is introduced in (2.2.2). For investigating the effects of slow parameter changes (for instance, a change in ring voltage) on a periodic ion motion, adiabatic invariants can be used (2.2.1). If these methods are not applicable, one can always numerically integrate the equations of motion as a last resort.

2.2.1 Adiabatic Invariants

For periodic motions, a change of external parameters (in our case: the ring voltage V_0 or magnetic field $\vec{B}$) is called slow or adiabatic, if the relative change of the parameters is much slower than any of the frequencies of the periodic motion. For these slow changes it can be shown [23] that the integrals

$$I_i = \frac{1}{2\pi} \oint p_i dq_i \tag{2.24}$$

are constants of the motion called "adiabatic invariants". The variable p_i is the canonical momentum in the Hamilton formalism, and q_i the corresponding generalized coordinate. The closed integral is executed over the path of the particle for a fixed value of the external parameter. Performing these integrals for a particle in a Penning trap,

three adiabatic invariants [24] can be calculated - one for each canonical momentum. These adiabatic invariants can be identified with

- $I_z = \frac{E_z}{\omega_z}$: the ratio of Energy in the axial mode to the axial frequency,
- $I_+ = \mu_c = \frac{1}{2} q \omega_+ \rho_+^2$: the magnetic moment of the cyclotron motion,
- I_-: The magnetic flux through the area enclosed by the magnetron orbit [25].

This allows us to estimate the change of motional radii, when we ramp the ring voltage between the $-87\,\mathrm{V}$ needed for precision experiments, and $-0.5\,\mathrm{V}$ needed for ion transfers.

2.2.2 Guiding Center Motion

In strong magnetic fields, charged particles perform a fast cyclotron motion perpendicular to the direction of the magnetic field. If the radius of this motion is much smaller than the lengthscales, in which the electric and the magnetic fields change, we can introduce a system of coordinates that separates the ion trajectory into a fast cyclotron motion and a slow motion of the center of the cyclotron orbit [26]. This cyclotron center $\vec{R}$ is also called the "guiding center". By averaging the ion motion over each cyclotron period, the influence of the fast cyclotron motion on the guiding center motion averages out to first order, except for a term that is proportional to the magnetic dipole moment of the cyclotron motion. Since this dipole moment $\vec{\mu_c}$ is an adiabatic invariant of the ion motion, the averaged equations of motion can be written as:

$$\ddot{\vec{R}} = \frac{q}{m}\left(\vec{E} + \dot{\vec{R}} \times \vec{B}\right) - \frac{1}{m} |\vec{\mu_c}| \, \vec{\nabla} \left|\vec{B}\right| \quad . \tag{2.25}$$

The right hand term is the familiar coupling of a magnetic moment to an inhomogeneous magnetic field. Absolute values appear in this term, because the magnetic moment of the cyclotron motion is always antiparallel to the magnetic field, so some of the vector products evaluate to a product of absolute values. Another simplification lies within the "averaged" start parameter $\dot{\vec{R}}_0$. Let $\vec{v}_\parallel$ be the velocity component parallel to the magnetic field and $\vec{v}_\perp$ be the velocity component perpendicular to the field. Then most of $\vec{v}_\perp$ is averaged to zero by the cyclotron motion, and the start parameter

is largely dominated by $\vec{v}_{\parallel}$:

$$\dot{\vec{R}}_0 = \vec{v}_{0\parallel} + \frac{\vec{E} \times \vec{B}}{\vec{B}^2} \quad . \tag{2.26}$$

The second term is a slow $\vec{E} \times \vec{B}$ drift. In a Penning trap, this drift can be identified with the magnetron motion.

If the magnetic field gradient is small, the force due to the coupling of $\vec{\mu_c}$ to $\vec{\nabla} \left| \vec{B} \right|$ is negligible and the equations of motion can be further simplified . The motion along the magnetic field lines becomes independent from the perpendicular motion and can be treated in a one dimensional fashion, while the perpendicular motion can be fully described by the $\vec{E} \times \vec{B}$ drift.

$$\dot{\vec{R}}_0 = \vec{v}_{0\parallel} + \frac{\vec{E} \times \vec{B}}{\vec{B}^2} \tag{2.27}$$

Chapter 3

Experimental Setup

The experiment was first designed and built at the University of Washington in Seattle by the group of Robert S. Van Dyck, Jr. One goal of the design was to stabilize the magnetic and electrostatic fields as much as possible. For this purpose, a superconducting magnet system [27] and a precision voltage source [28] were custom built. Further, the experiment features an external ion source and a double trap setup. This will help to decrease the time between frequency measurements of the reference ion and the ion of interest, which will in turn lower the impact of external fluctuations. A detailed description of the majority of the hard- and software used in the experiment can be found in the thesis of David Pinegar [21], who designed much of the electronics of this setup.

In 2008, the experiment was moved to the Max-Planck-Insitute for Nuclear Physics in Heidelberg, where a new lab has been set up to meet the specific requirements for this setup. The magnet was placed on a vibrationally isolated platform in a temperature stabilized room, and the laboratory was equipped with the proper safety measures to allow secure handling of the radioactive tritium.

The next two chapters will give an overview of the hardware that is used in the ion transfers from the ion source to the traps, and in the transfers between the traps. This chapter will focus on the ion source and mechanical layout of the beamline, which includes trap dimensions and the system that allows us to position the trap inside the magnet bore. The transfer sequences and the corresponding electronics will be presented in the next chapter.

3.1 Beamline Overview

The beamline, which is schematically shown in figure (3.1), is mounted vertically. It can be lifted in and out of the cold bore of the superconducting magnet via a crane system. It mainly consists of a Penning ion source at the top, a 130 cm long transfer tube, and two hyperbolical Penning traps at the bottom. The ion source and the beam tube are separated by a computer controlled "gate valve", which is opened only for ion loading. The lower end of the beam tube is connected to the trap envelope via a flexible bellows. Through rotation of four control rods parallel to the beam tube, the trap envelope can be shifted by several mm and tilted by up to 2.4° relative to the magnet bore. The tilt angle allows us to align the trap axis with the magnetic field axis, while the x–y translation can be used to shift the traps into the ion beam center.

In order to stabilize the trap temperature, the liquid helium level inside the bore is kept 30 cm above the traps at a stabilized pressure. This is important, because the magnetic susceptibilities of the materials used in the high B-field region are temperature dependant. A fluctuation in temperature would therefore change the effective magnetic field at the ion's position. Further measures to stabilize the field have been taken, which are described in detail in [27] and will be presented in an upcoming thesis[1].

3.2 Penning Ion Source

The ion source is schematically pictured on the left hand side of figure 3.2. This type of ion source is called a Penning ion source[29], because its layout resembles a Penning vacuum gauge[11]. It creates ions from neutral gas by electron impact ionization. It features an axial magnetic field to increase the total travel distance of the electrons, thereby increasing the likelihood of ionization events. In our setup this magnetic field consists of the fringe field of the superconducting magnet, and the variable field of an additional solenoid that is wound around the vacuum envelope of the ion source.

[1] Sebastian Streubel, 2012

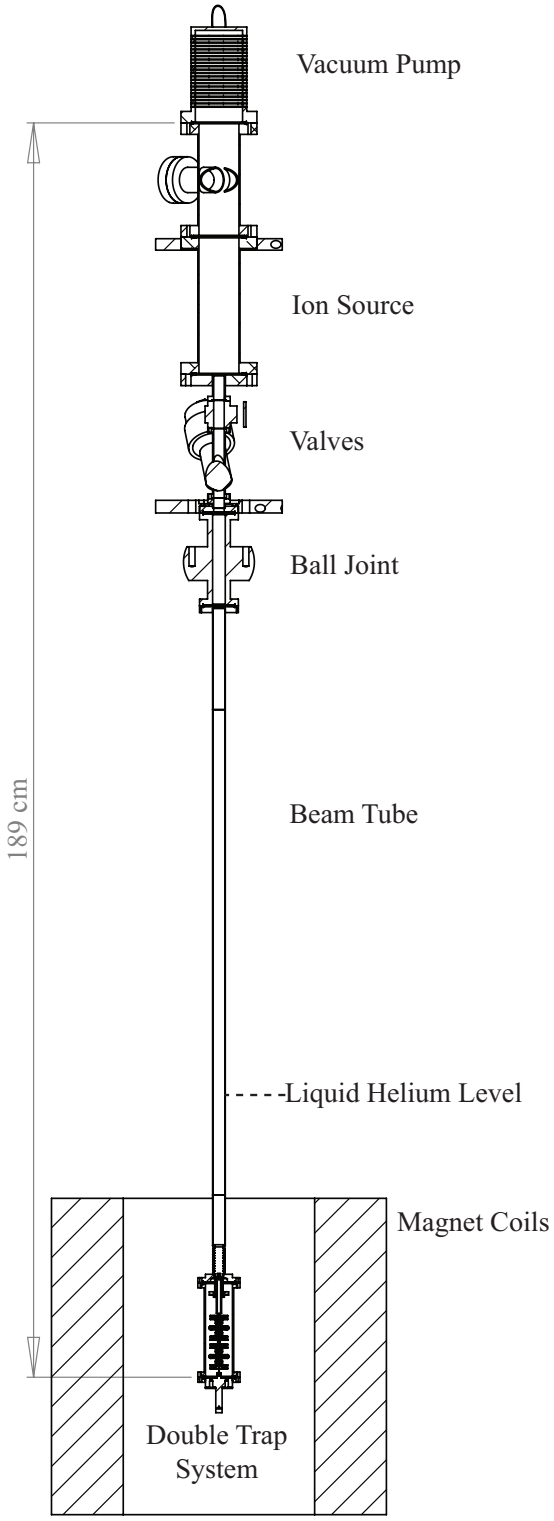

Figure 3.1: Beamline overview. When the experiment is lowered into the magnet, everything below the ball joint is surrounded by the magnet cryostat. Not shown are the various electrical feedthroughs, the detection electronics, and the "translation/tilt stage" which allows us to shift and tilt the trap envelope inside the magnet bore.

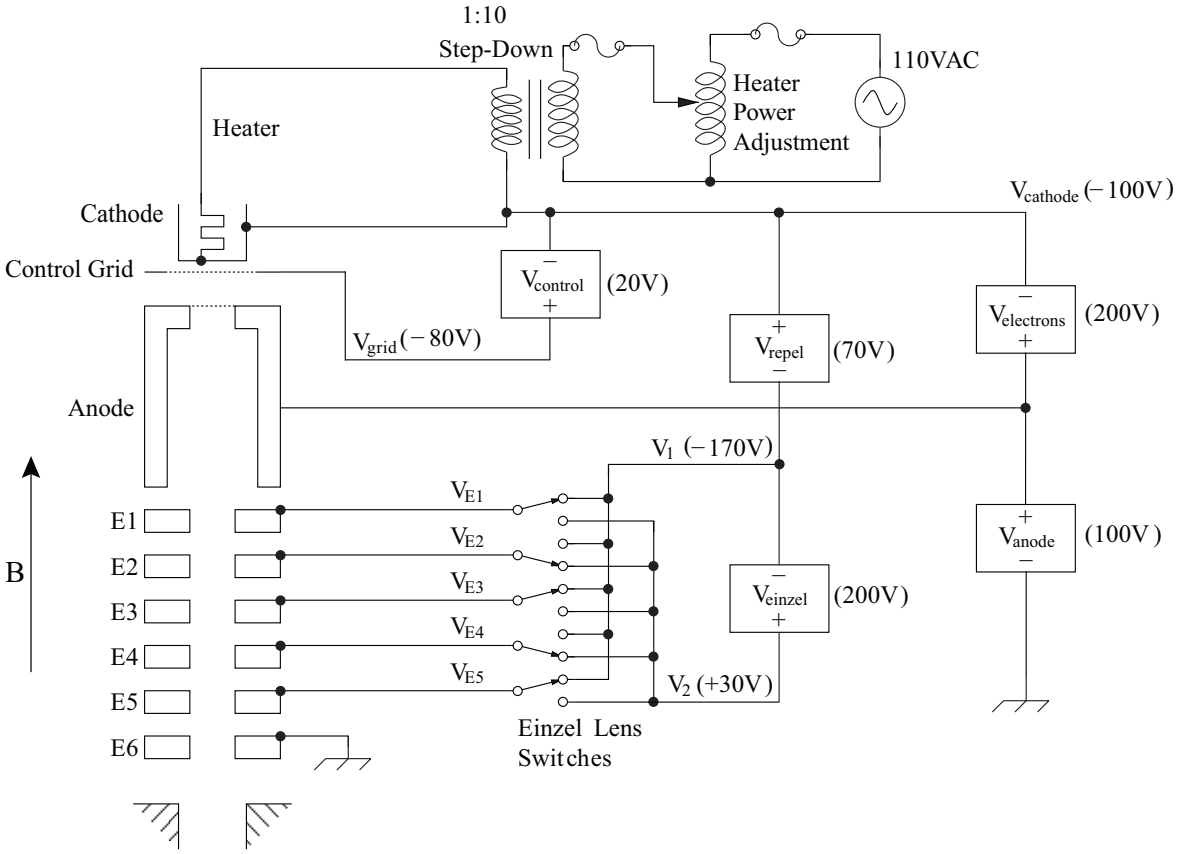

Figure 3.2: Electrical schematic of the ion source. Power supplies are pictured as boxes, with typical voltage settings given next to them. All power supplies except V_{anode} are floating with respect to ground. The resulting voltages V_{cathode}, V_{grid}, V_1 and V_2 are given with respect to ground.

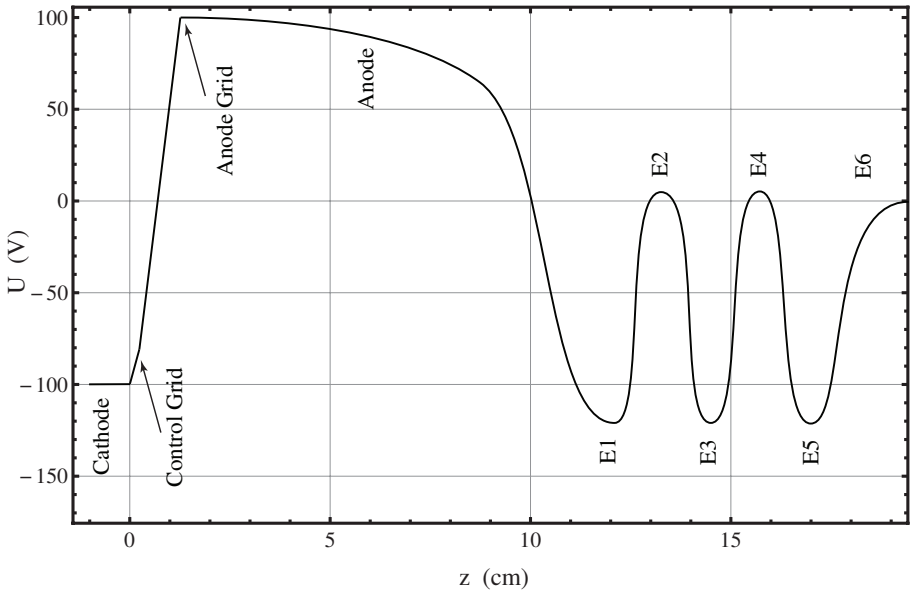

Figure 3.3: Schematic of the electrostatic potential along the ion source axis (not to scale). This potential corresponds to the Einzel lens switch positions shown in figure 3.2.

3.2.1 Primary Electrons

The primary electrons necessary for the impact ionization are emitted from a heated, barium coated tungsten cathode. A control grid pulls the electrons away from the cathode and accelerates them towards the anode. The voltage V_{control} between control grid and cathode can be used to regulate the electron current, while the voltage $V_{\text{electrons}}$ between cathode and anode determines the kinetic energy of the electrons inside the anode. The top of the anode tube is covered by another grid, which enhances the shape of the axial potential (see figure 3.3, explanation below). On the far side of the anode the electrons are reflected by the first Einzel lens, which is biased with V_{repel} below the cathode voltage. The anode tube is open at the bottom, so that the fringe field of the first Einzel lens creates a small potential gradient inside the anode towards the Einzel lens stack. Eventually, the electrons are collected by either the anode, the anode grid, or the control grid.

3.2.2 Ion Creation

By opening precision needle valves for a short time (approximately 20 s), minute quantities of neutral ^{3}H or ^{3}He gas can be flowed into the anode tube. The primary electrons

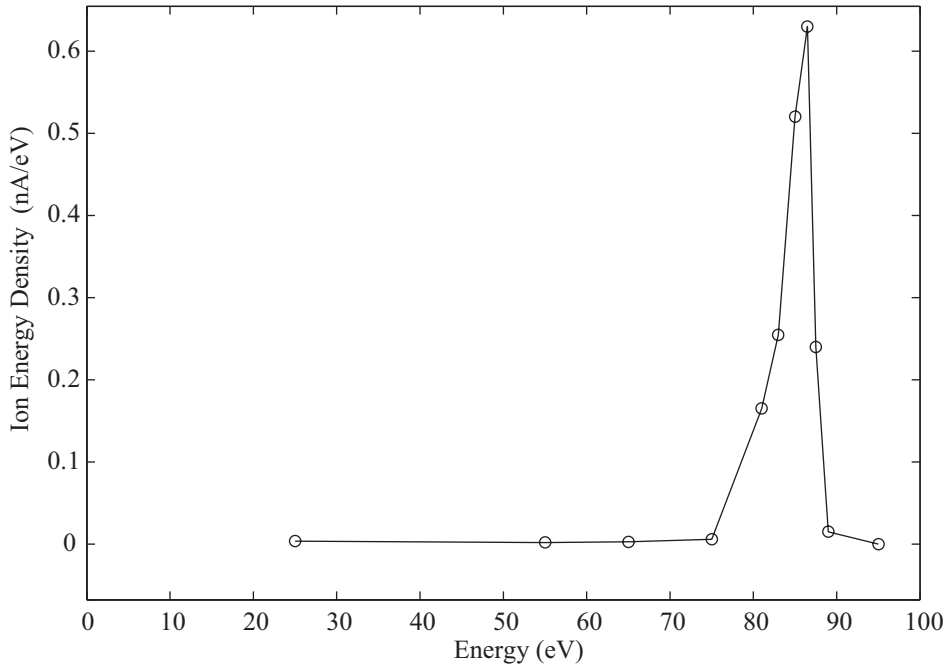

Figure 3.4: Energy distribution of ions from the ion source, courtesy David Pinegar. The anode voltage was set to $V_{\text{anode}} = 100\,\text{V}$ for this measurement. The maximum energy of the ions is 10 eV lower, because the charge density of the electron current ($I_{\text{electrons}} = 10\,\text{mA}$ in this example) effectively reduces the potential inside the anode. The ionized neutral gas consisted mostly of outgassing (water, oxygen, hydrogen) from the cathode, at a pressure of $\approx 8 \times 10^{-7}\,\text{mbar}$. The effect of outgassing decreases significantly after running the ion source for about one hour.

ionize parts of this gas and create, for V_{anode} between 50 V and 200 V, mostly singly charged ions [30]. The majority of these positively charged ions are ejected out of the anode towards the Einzel lens stack by a small potential gradient (as sketched in figure 3.3), which is due to the field from the negatively charged Einzel lens E1. The Einzel lenses can be biased with either V1 or V2 to electrostatically focus the ion beam down into the beam tube. Experiments by the Seattle group have shown that approximately 40 % of the created ions hit the first Einzel lens, while the majority of the remaining 60% leaves the Einzel lens stack towards the beam tube. A typical value for the current of this ion beam is about 70 nA.

3.2.3 Ion Source Voltage Supplies

The voltages for the ion source electrodes are given by a network of power supplies that bias most electrodes relative to one another (see right hand side of 3.2). Compared to biasing each voltage relative to ground, this setup has two main advantages:

- Power supply requirements: The electron beam current I_{electron}, which is of the order of 10 mA, flows mostly between anode and cathode. By biasing V_{electron} relative to V_{anode}, I_{electron} flows through one power supply instead of two. This is preferable, because high voltage power supplies capable of such a current tend to be bulky and noisy.

- Current measurement: The ion beam current I_{ion} is several orders of magnitude smaller than the electron beam current. In a non-floating setup, I_{ion} would be masked by I_{electron}, whereas our setup allows us to measure I_{ion} directly. Because there is only one pathway to ground on the electrode biasing network, conservation of charge dictates that I_{ion}, which leaves the ion source, must be compensated by current entering through the V_{anode} power supply.

3.3 Translation/Tilt Stage

The translation/tilt stage for the adjustment of the tilt angle and the position of the two Penning traps is manipulated through four control rods, as shown in figure 3.5. They are situated parallel to the beamline and can be rotated from outside of the magnet cryostat. The rods that control the trap translation are labeled T1 and T2; those that control the tilt are labeled R1 and R2.

It is best to view the translation/tilt stage as two separate systems: The x–y translation stage that shifts the trap, and the tilt stage, which tilts the trap and is located beneath the x–y translation stage.

3.3.1 x–y Translation Stage

Four small posts radially protrude the x–y translation stage (see right hand side of figure 3.5). Two of them are spring-loaded and push against the inner wall of the

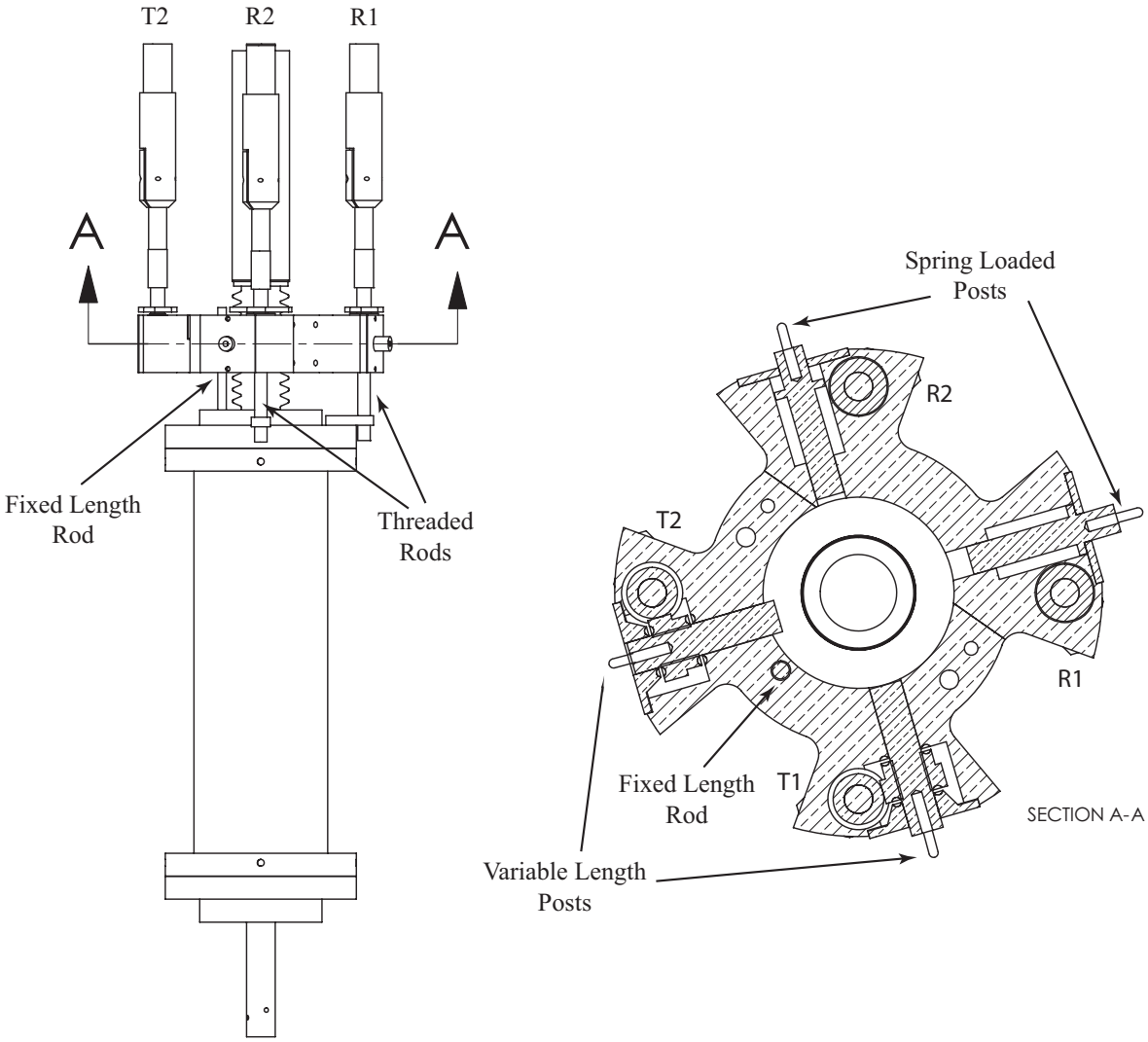

Figure 3.5: Details of the translation/tilt stage. Turning T1 counter clock-wise reduces the length of the adjacent post, letting the spring loaded post on the other side push the trap center towards T1. The tilt stage consists of three rods that are arranged in a equilateral triangle. R1 and R2 control the effective length of two of these rods, which can be used to tilt the vacuum envelope of the traps relative to the x–y translation stage.

magnet bore tube. The length of the other two posts can be changed by rotating the control rods T1 and T2. By turning T1 or T2 one full revolution counter clock-wise (ccw), the length of the corresponding post decreases by 39.6 μm. This shifts the trap envelope towards this post, while keeping the trap tilt — to first order — constant.

3.3.2 Tilt Stage

The tilt stage can be thought of as three rods that connect the x–y translation stage with the trap envelope. Two of these rods are the threaded ends of R1 and R2. The third rod has a fixed length and is slightly flexible. Viewed from above, these rods are arranged in an equilateral triangle. R1 and R2 are held in place inside the x–y translation stage by ball bearings, which allow them to rotate freely, but fix the x–y translation stage in a horizontal position.

The threaded ends of R1 and R2 are screwed into tapped holes of two metal plates, which are fixed to the trap envelope. By rotating R1 or R2, the distance between the x–y translation stage and the trap envelope along this rod changes, thereby tilting the trap. One ccw rotation of R1 or R2 tilts the trap 1° away from the rod being turned.

For beam alignment, it is important to remember that tilting the trap also changes the x–y position of the first small-diameter hole that the beam encounters (the hole inside the CtSkim electrode, see 3.4). This can be compensated with the x–y translation stage:

- One ccw turn of R1 can be compensated by 19 ccw turns of T1 and 32 cw turns of T2.
- One ccw turn of R2 can be compensated by 37 cw turns of T1.

The maximum trap tilt is limited by the 10 cm magnet bore tube diameter: At a tilt of 2.4°, the lowest part of the beamline hits the wall of the magnet bore.

3.3.3 Tilt Plots

In our setup, we call diagrams, that show measurements as a function of the R1 and R2 control rod position, “tilt plots”. For instance, we can plot which positions of R1 and R2 correspond to moving the bottom of the trap in a circular motion (see figure 3.6).

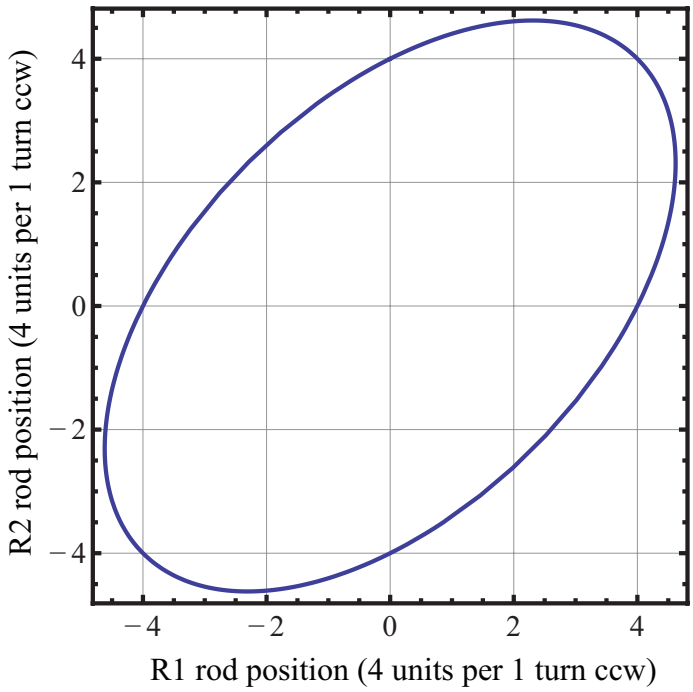

Figure 3.6: A basic tilt plot depicting which positions of the R1 and R2 control rods correspond to the trap being tilted by 1°.

Since the tilt-changes caused by R1 and R2 are not orthogonal, the circular motion is given by an ellipse in the tilt plot. Basic linear algebra yields the equation:

$$r_1^2 + r_1 r_2 + r_2^2 = x^2 \quad , \tag{3.1}$$

with r_1 and r_2 measuring the ccw turns of R1 and R2 from an arbitrary Null, and x giving the "diameter" of the circle in degrees of trap tilt.

3.4 Penning Traps

The lower of the two hyperbolical traps is placed in the center of the magnet bore, where the field is most homogeneous. This is the trap used for precision experiments and is called the “experiment trap”. The other trap, called “capture trap”, can be used for storing another single ion of interest or single reference ion. It can also be utiliized for separate ν_z measurements to monitor the stability of the ring voltage.

Figure 3.7 shows a cutaway view of the trap electrodes. Each trap consists of a ring electrode, two endcaps and four guard electrodes. These guard electrodes are biased with a experimentally determined dc-voltage to compensate perturbations of

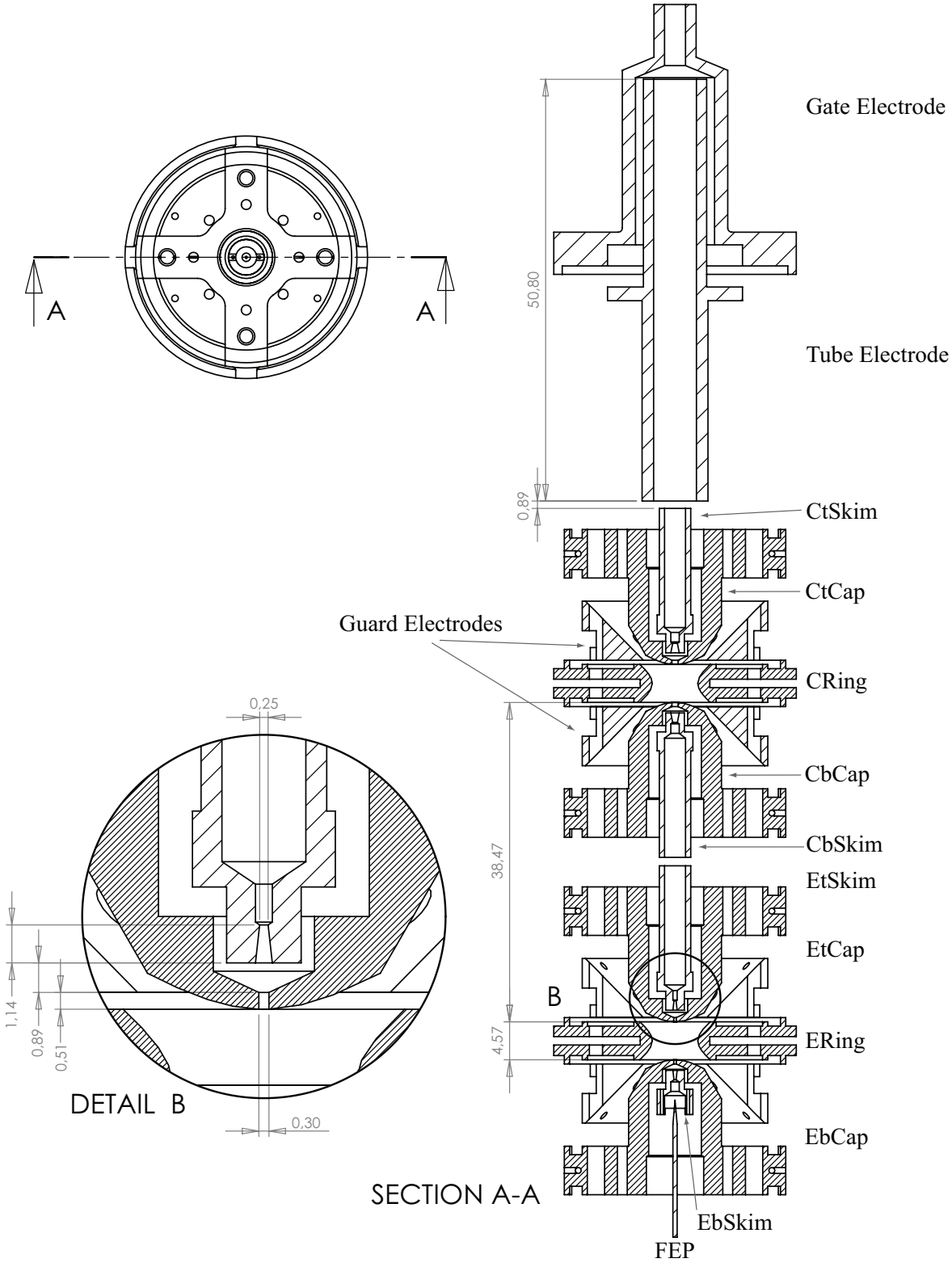

Figure 3.7: A detailed schematic of the trap electrodes, including the field emission point (FEP). All dimensions given in mm. Note: The holes of the top trap endcaps and skimmers are twice the diameter of the corresponding bottom trap electrodes.

the quadrupolar electrostatic field. They are also used to couple RF signals into the trap in order to manipulate the ion motion. The naming scheme of the electrodes is as follows: The first letter (C or E) stands for capture or experiment trap, the second letter (t or b) for top or bottom. The remaining letters give the electrode type. EtCap, for instance, stands for the top endcap of the experiment trap.

Each endcap has a hole in its center, through which the ions are transported. The diameters of the holes in CtCap and CbCap measure 0.74 mm, while the holes in EtCap and EbCap are more than a factor smaller (0.30 mm) to keep electrostatic field perturbations to a minimum.

Located above and below each trap are so called "skimmer electrodes". They can be thought of as bottlenecks, which collect off-axis ions and electrons during transfers. This reduces the chance that surface charge builds up on the endcaps, caused by stray electrons and ions. These bottlenecks are even smaller in diameter than the endcap holes, measuring 0.57 mm for the capture trap skimmers and 0.25 mm for the experiment trap skimmers.

A third, non-precision Penning trap, called the "tube trap", is located above the capture trap. Instead of a hyperbolical ring electrode, it features a larger, cylindrical tube electrode. The endcaps are also not hyperbolical, but formed by CtSkim on the bottom and another electrode, called the "gate electrode", at the top. This trap has no detection circuitry attached and is used for storing a larger number of ions ($\approx 10^6$) from the ion source.

3.5 Ion Detection

Figure 3.8 shows a rough sketch of the ion detection system, which is set up as a feedback loop. Only the axial ion movement is detected directly. It induces an image current of some fA in the endcaps, which is used to excite a resonant LC circuit[31]. The signal is amplified further by several cryogenic and room temperature amplifiers [21]. By comparing the 4 MHz ion signal to a reference frequency, changes in the ion frequency are detected and turned into a correction signal. This correction signal is then added to the ring voltage in order to lock the axial frequency at 4 MHz. Since the

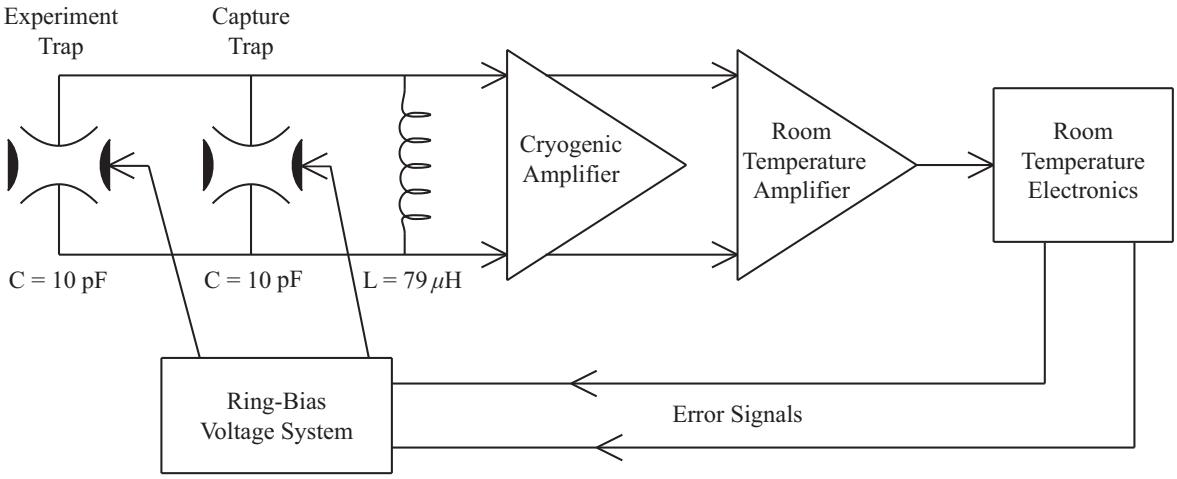

Figure 3.8: Sketch of the Detection Circuit. The 4 MHz axial ion motion excites a resonant LC circuit. The resulting voltage drop is amplified in several stages and compared to a reference frequency to detect changes in the ion axial frequency. These changes are converted to error signals that are fed back onto the ring electrodes, which locks the ion's axial frequency at 4 MHz.

axial frequency depends slightly on the energy in the magnetron and cyclotron mode, the correction signal changes, if these modes are excited with RF signals of the correct frequencies.

For a good signal-to-noise ratio, the image current of the axial motion must cause the highest voltage drop possible across the endcaps, which can be achieved by minimizing the capacitance of the tuned circuit. Consequently, the LC circuit consists of a 79 μH coil and the endcaps, which act as capacitors. At cryogenic temperatures, the quality factor of this circuit lies between 500 and 1000. Care must be taken to minimize any additional capacitance to ground. In a simplified model, any capacitance to ground would allow parts of the RF image current to bypass the LC circuit, thus reducing the voltage drop across the endcaps.

The details of the electronic detection circuit was not the main focus of this thesis — a more detailed description of the amplifier system is not given, since it goes beyond the scope of the work presented here.

Chapter 4

Ion Loading and Transfers

The Seattle group investigated the loading of the traps through simulations and experiments [21]. They also devised a scheme to transfer ions between the two hyperbolical traps, but this "trap-to-trap" transfer has not yet been investigated in detail. It is probably the most challenging of the transfer sequences, because the ions have to pass through holes that are only 250 μm in diameter.

This chapter addresses those parts of the experiment that are directly related to the ion transfers. After an overview of the three different transfer types, they are explained in detail in sections 4.2 to 4.4. Section 4.5 contains information about the diode-drive-RF system, which allows us to switch the impedance of certain electrodes between approximately 50 Ω to transmit pulses, and more than 10 MΩ for precision ion measurements. In the last section, an overview over the pulse box and electrode termination will be given.

The feasibility of the trap-to-trap sequence will be discussed in chapter 6, using the results of the commissioning experiments (chapter 5).

4.1 Transfer Sequence Overview

Three transfer sequences are needed to move ions from the ion source into the experiment trap.

1. The "initial-load" sequence is used to load ions from the ion source into the tube trap. This sequence also reduces the mean kinetic energy of the ions from 90 eV

Table 4.1: Overview of the transfer voltages

Voltage	Value	Description
V_{anode}	100 V	repels the 90 eV ion beam
V_{cutoff}	87 V	slows down ion beam
V_{well}	-0.5 V	well depth of tube trap
$V_{extract}$	-4 V	extracts ions out of tube electrode
$V_{transfer}$	-0.5 V	slowly extracts ions out of hyperbolical traps
V_{drift}	-4.0 V	speeds up the trap-to-trap transfer
V_{0p}	-87 V	ring voltage for precision measurements
V_{0t}	-0.5 V	ring voltage for transfers

to 3 eV, and then removes all ions with a kinetic energy higher than 0.5 eV.

2. The "tube-to-trap" sequence moves a small number (0 to 10) of ions from the tube trap into the capture trap.

3. The "trap-to-trap" sequence is designed to transfer small number of ions (or even single ions) between the capture trap and the experiment trap. In principle, it could also be used to swap single ions between the traps simultaneously. By storing a ^{3}H ion in one trap, and a ^{3}He ion in the other, this would allow us to reduce the time between precision measurements on different ion species from hours down to minutes.

During precision measurements the skimmer electrodes are grounded. The rings are biased with V_{0p}, the voltage from our precision source [28], and the gate electrode is biased with V_{anode} to reflect the ion beam. The potential of the tube trap is held at $V_{well} = -0.5$ V to keep low energy ions trapped.

During operation of the ion source the computer controlled gate valve is usually closed, in order to protect the trap vacuum from ion source outgassing. It is only opened during the initial-load sequence to allow the ion beam to reach the traps.

The next three sections describe details of the transfer sequences. For quick reference, an overview of all voltages used during the transfers can be found in table 4.1, while table 4.2 summarizes the sequences as they were devised by the Seattle group.

Electrode	Idle	Initial-Loading	Tube-to-Trap	Trap-to-Trap
gate valve	0 V	25 V for 1 s		
gate elec.	V_{anode}	V_{cutoff} for 0.875 s		
tube elec.	V_{well}	V_{cutoff} for 2 s		
CtSkim	0 V	V_{anode} for 2.5 s	$V_{extract}$ for 1.5 μs*	
CtCap	0 V		$V_{transfer}$ for 1.5 μs*	
C Ring	V_{0p}		V_{0t}	V_{0t}
CbCap	0 V			$V_{transfer}$ for 5.8 μs*
CbSkim	0 V			V_{drift} for 50 ms
EtSkim	0 V			V_{drift} for 50 ms
EtCap	0 V			$V_{transfer}$ for 5.8 μs*
E Ring	V_{0p}			V_{0t}
EbCap	0 V			
EbSkim	0 V			

Table 4.2: Overview of the transfer sequences. Entries marked with * are superimposed with the diode-drive-RF signal (see section 4.5), and blank entries correspond to electrodes that are idle during a particular pulse.

4.2 Initial-Load Sequence

At the optimal settings, an ion current of approximately 70 nA leaves the ion source with an energy of about 90 eV. The Seattle group estimated through simulations that, once the gate valve is opened, 93 % of this ion beam hits the beamtube as it travels down towards the center of the magnetic field and is lost. The ion loss is expected to be slightly higher in the Heidelberg setup, because the magnet was charged to only 5.3 T instead of the 5.9 T that were used for the simulations studies. However, all ions that do not hit the beamtube will be focused by the magnetic field to within 0.5 mm of the beam axis. This is well below the 2.5 mm inner diameter of the gate electrode (see section 3.4).

The kinetic energy of the ions inside the grounded beamtube is given as the potential difference between their point of creation and ground. Measurements have shown that the primary electron beam reduces the potential inside the anode by several volts (see figure 3.4). The energy spread of approximately 5 eV is dominated by the potential gradient inside the anode. The measured energy plot was taken with the beamline outside of the superconducting magnet. It should be kept in mind that the axial energy of the ions that travel to the inside of the magnet can be reduced by up to 10 eV due to the magnetic mirror effect. Since this energy loss depends on the start conditions of the ions (radial offset, radial velocity component), the energy distribution of the ions in the strong field region is also broadened. It was shown, however, that more than 1 % of the total ion current can be focused well enough to keep the energy loss below 5 eV.

The initial load sequence starts by biasing CtSkim with V_{anode}, and the tube electrode with a voltage called V_{cutoff} (see figures 4.1). Because both electrodes have large RC times of 0.1 s, a one second delay allows them to charge up to the given voltage.

The gate valve is then switched to “open” and the gate electrode pulsed to the same voltage as the tube electrode, which is V_{cutoff}. There is a mechanical 0.25 second delay of the gate valve, pictured in figure 4.1 is the electric pulse. By setting V_{cutoff} a few volts below the mean ion beam energy, the kinetic energy of the ions decreases and the ion density increases. The ion beam is deflected on the bottom side of the tube electrode by the CtSkim electrode. After 0.875 s the gate valve is closed again and the

gate electrode pulsed up to V_{anode}, which traps all ions that are inside the tube trap at that moment. 0.125 s later, the voltage of the tube electrode is gradually reduced to $V_{\text{well}} = -0.5\,\text{V}$, which in turn reduces the potential energy of the trapped ions. After 1.0 s, the voltage of CtSkim gradually returns to ground. All ions with a kinetic energy greater than 0.5 eV (given by V_{well}) will now be lost, leaving an estimated one million ions with an energy range between 0 eV and 0.5 eV inside the tube trap.

4.3 Tube-To-Trap Sequence

The tube-to-trap sequence is designed to load a small number of ions into the capture trap, while minimizing the total ion loss. Because the ions have to pass through a hole inside the CtSkim electrode, that is only 570 μm in diameter, the ions are transferred in a fast, single pass transfer, instead of letting the ion densities equalize in the two traps. By pulsing down the CtSkim electrode from ground to $V_{\text{extract}} = -4\,\text{V}$ for several μs, some ions will be extracted out of the beam tube and travel quickly towards the capture trap. At the same time, the top endcap of the capture trap, CtCap is pulsed down to $V_{\text{transfer}} = -0.5\,\text{V}$, which allows the ions to enter the trap (see figure 4.2).

By using the ring voltage $V_{0\text{t}} = -0.5\,\text{V}$ for transfers instead of the precision measurement voltage $V_{0\text{p}} \approx -87\,\text{V}$, the potential well inside the capture trap is less deep and has a smaller gradient. Ions that enter the trap are accelerated more slowly by this gradient, and thus spend more time in the trap. This lessens restrictions on the exact pulse length.

Because there is no detection circuit attached to the tube trap, the ions are not cooled significantly. They occupy a very broad energy range between 0 eV and 0.5 eV, the maximum given by $V_{\text{well}} = -0.5\,\text{V}$. To minimize ion loss of this sequence, the pulse length should be as short as possible. An estimation yields that at a pulse length of about 1.5 μs, a Poisson-distributed number of ions will be transferred, and about 10 % of ions from the tube trap will be lost with each transfer attempt.

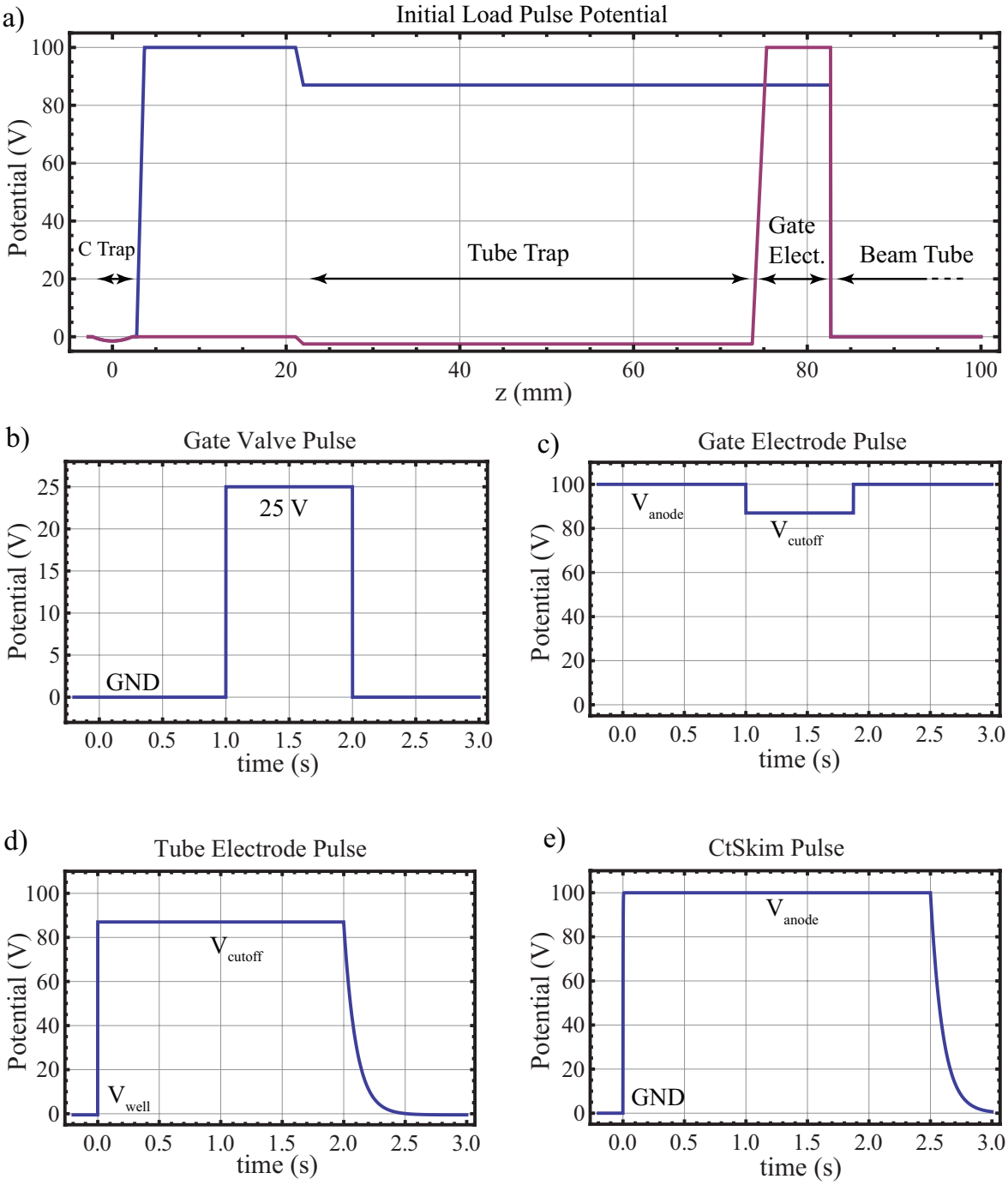

Figure 4.1: Pulse overview of the initial-load sequence. Figure a) shows the potential along the z-axis during the pulse in blue, and before/after the pulse in purple. The z-coordinate is given from the center of the capture trap. Figures b) through e) depict the individual electrode pulses in the time domain. Figures d) and e) show how the potential of the tube electrode and CtSkim are lowered gradually at the end of the pulse, which adiabatically reduces the potential energy of the ions.

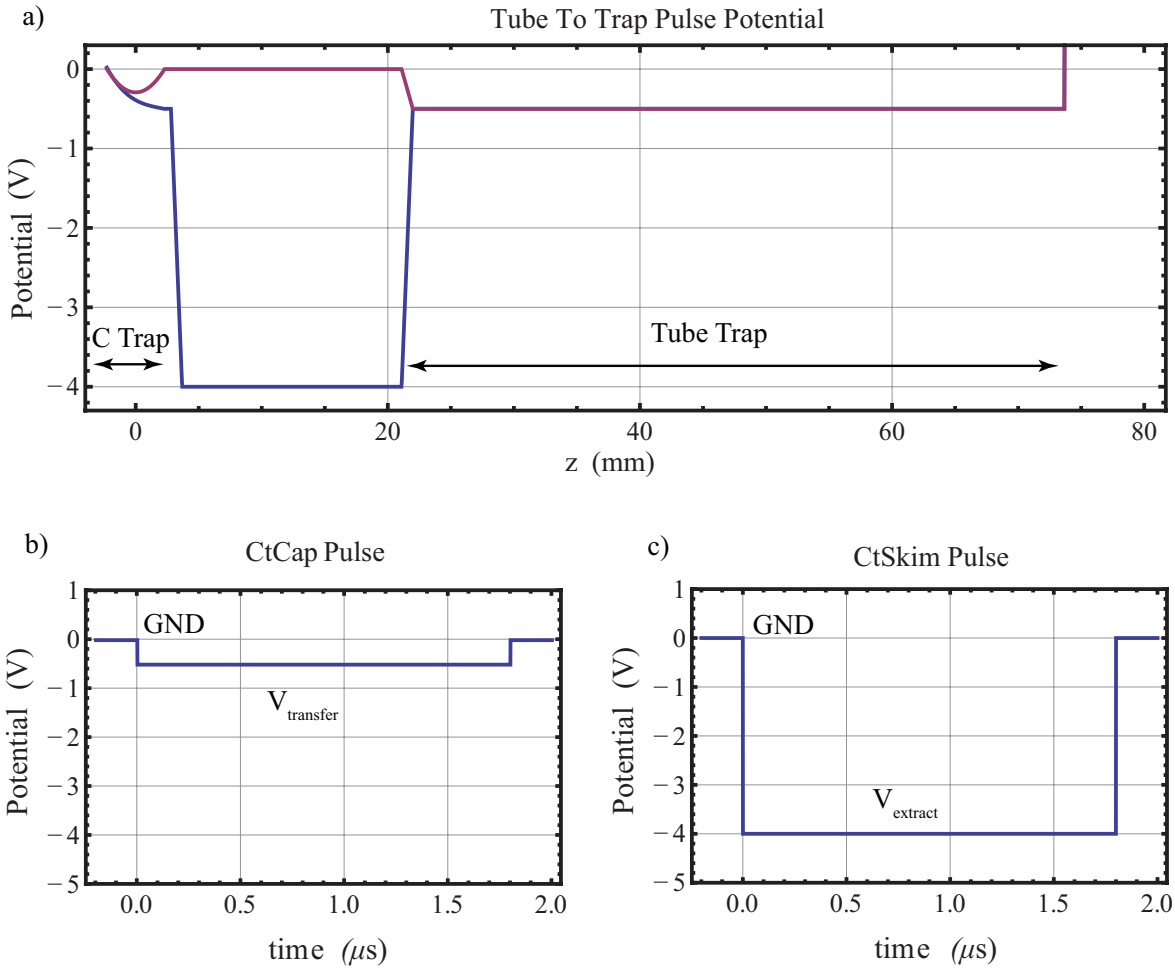

Figure 4.2: Pulse overview of the tube-to-trap sequence. Figure a) shows the pulse potential along the z-axis during the pulse in blue, before/after the pulse in purple. This sequence involves only two electrodes; their ideal pulse shapes in the time domain are given in figures b) and c).

4.4 Trap-To-Trap Sequence

For the same considerations noted for the tube-to-trap sequence, the trap-to-trap sequence is also a single-pass transfer. The same ring voltage $V_{0t} = -0.5\,\mathrm{V}$ is used. The sequence begins by pulsing the skimmer electrodes down to $V_{\mathrm{drift}} = -4\,\mathrm{V}$. They are allowed to charge to this voltage for 40 ms, at which point the endcaps are quickly pulsed down to $V_{\mathrm{transfer}} = -0.5\,\mathrm{V}$. The small potential gradient extracts the ions out of one trap towards the skimmer electrodes within 1.4 μs.

The skimmer electrodes accelerate the ions, to lessen the influence of surface patch potentials on the ions. Surface patch potentials create electric fields perpendicular to the ion motion that move the ion away from the trap axis. However, a voltage V_{drift} that is different from V_{transfer} causes radial electric fields between the endcaps and the skimmer electrodes, which can also defocus the ion path. $V_{\mathrm{drift}} = -4\,\mathrm{V}$ was chosen as a compromise between these effects.

The ions are slowed down by the endcap of the other trap, where they are slowly reflected within 2.8 μs. At the exact moment when they are at rest in the center of the other trap, the endcaps are pulsed up to ground again, which traps the ions.

4.5 Diode-Drive-RF System

Because the endcap electrodes are used to detect the axial ion motion, any external connection to them must be of very high impedance (many MΩ), in order to not spoil the resonant LC circuit (see section 3.5). For ion transfers, on the other hand, they need to have a low impedance. Otherwise, a fast voltage pulse would

1. be distorted through RC filtering, and

2. excite the resonant LC circuit, causing 4 MHz "ringing" of the endcap potential.

An upper limit for the maximum allowed impedance can be derived by looking at an example for case 1.: Since the endcaps have a capacitance of about 20 pF to ground, the resistance between the pulse voltage source and the endcap must be below 50 Ω for a 1 ns RC time at the beginning and end of each pulse due to the RC filtering.

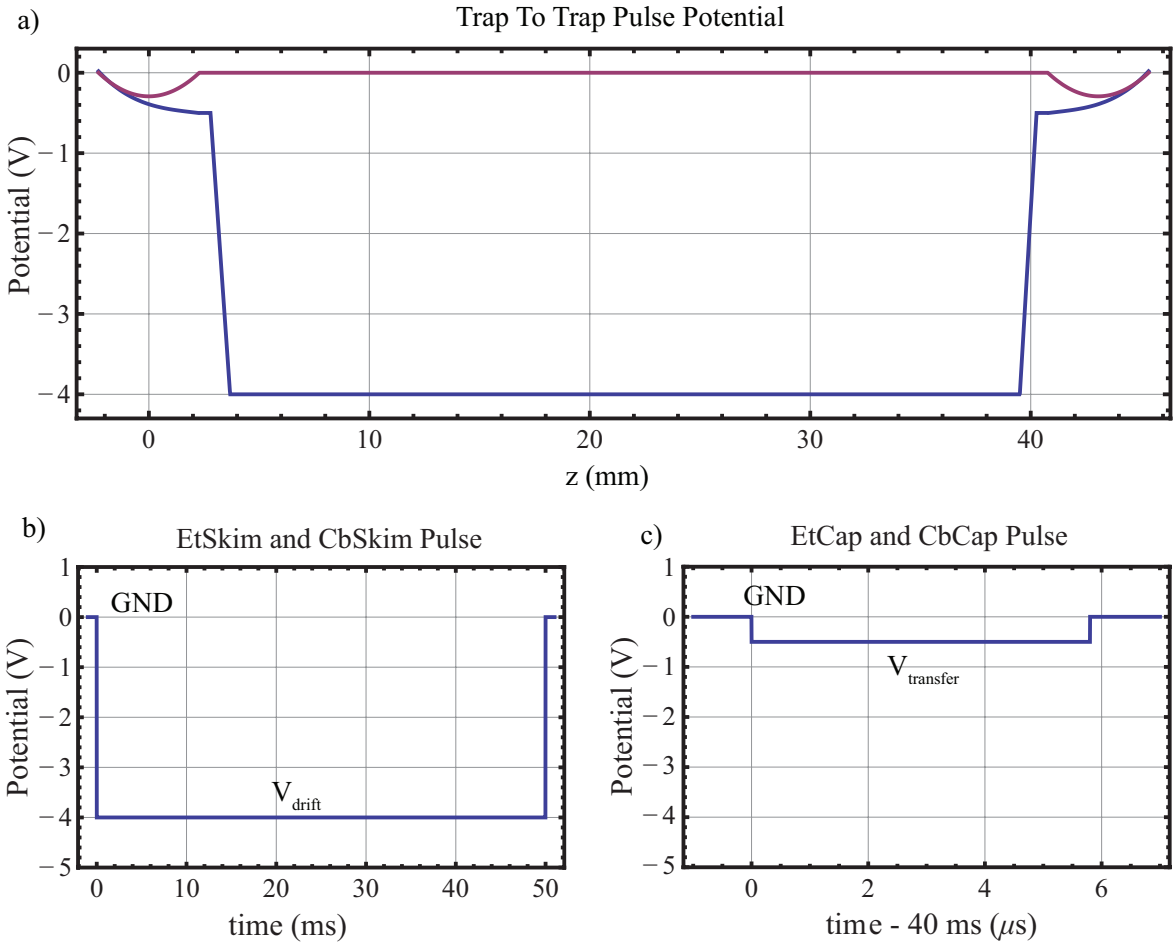

Figure 4.3: Pulse overview of the trap-to-trap sequence. Along the z-axis, this pulse is symmetric with respect to the center between both traps (figure a). This holds true for both during the pulse (purple curve), and before/after the pulse (blue curve). Four electrodes are pulsed in this sequence. Due to the symmetry, the pulse on EtSkim is the same as the pulse on CbSkim (figure b), and the pulse on EtCap is equivalent to the CbCap pulse (figure c).

For this reason, we need a system that switches the electrode's impedance. A mechanical switch outside the cryostat is not an option, because such a long electrical lead would couple a large amount of noise onto the very sensitive amplifier. It would also introduce too much capacitative coupling to ground onto the tuned LC circuit.

Our system is based on a small, antiparallel GaAs diode pair (model MGS902) between the electrodes and the pulse voltage supply (see figure 4.4, top). The voltage drop induced by the ion signal is of order nV and far below the diodes' forward voltage $V_F = 700\,\mathrm{mV}$. The diode pair therefore acts as a high impedance circuit element for signals with small amplitudes.

The impedance can be switched by superimposing an RF signal, called the diode-drive-RF, over the pulse we want to apply (see figure 4.4, bottom). By choosing the diode-drive-RF amplitude just below V_F, it is mostly blocked by the diode pair. However, a pulse will introduce an additional voltage drop across the diode pair. For 50 % of the diode-drive-RF cycle, one of the diodes will therefore be forward biased and lets current flow with a low impedance.

Several considerations have to be made when choosing the optimal diode-drive-RF frequency. A frequency that is too low is not effectively damped by capacitances to ground at the electrode side of the diode pair and so it would couple onto the endcaps. A frequency that is too high dissipates too much energy into the diodes, because the impedance of the electrodes to ground decreases with frequency, which could potentially destroy the diodes. The diode-drive-RF should also be far away from all of the natural frequencies of the trapped ion. For us, a frequency of about 40 MHz seems to be the optimal choice. The diode pairs we use are only $250\,\mu\mathrm{m}$ in size and introduce less than 0.1 pF of capacitance to ground in the LC detector circuit [32].

4.6 Pulse Box and Electrode Termination

The pulses are created by a custom built, computer controlled "Pulse Box". It takes the various bias voltages as inputs from DC power supplies, and lets the user control the pulses' start and end times with a resolution of 50 ns. The hardware is described in detail in the thesis of David Pinegar [21], but some adjustments have been made

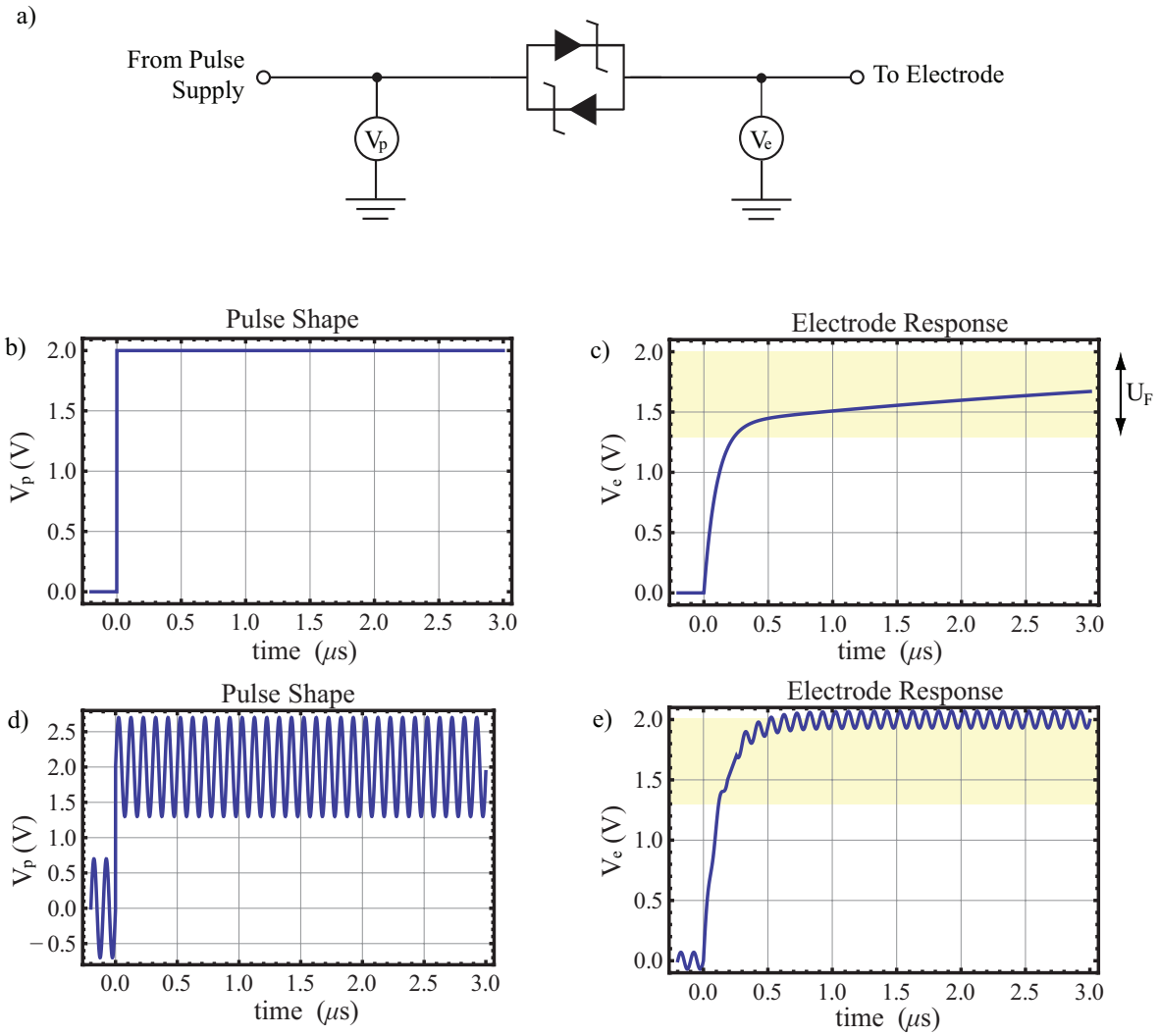

Figure 4.4: Influence of the antiparallel diode pair (figure a) on pulses, with and without diode-drive-RF. The top figures show a pulse V_p without diode-drive-RF in figure b), and a sketch of a typical electrode response V_e in figure c). As long as the voltage drop across the diode pair is larger than the diodes' forward voltage V_F, the pulse quickly charges the electrode. For a smaller voltage drop, only a small current can flow and the electrode charges slowly, as shown in the yellow region. Figures d) and e) show how the diode-drive-RF decreases the charging time, but weakly couples onto the electrode.

Table 4.3: Values of components used in figure 4.5

Component	Value	Description
R1	100 MΩ	limits the field emission point current
R2	100 MΩ	high impedance termination for slow pulses
D1	MGS902	anti parallel GaAs diode pair for impedance switching
C1	100 pF	passes 4 MHz ion signal, blocks DC voltage differences

in Heidelberg. Mainly, the termination inside the pulse box was modified to decrease reflections of the diode-drive-RF signal.

The pulse termination on the electrode side is shown in the schematic 4.5, with table 4.3 giving the corresponding component values. As mentioned above, the endcaps use the diode-drive-RF system. EbCap is not used in any transfer sequence, but it is also part of the diode-drive-RF system to keep both sides of the differential amplifier circuit symmetric.

The skimmer electrodes couple capacitively to the endcaps and consequently need to be of high impedance as well. Since only CtSkim needs to be biased with a fast pulse (during the tube-to-trap sequence), it is the only skimmer electrode connected via an antiparallel diode pair. The other skimmer electrodes are terminated with 100 MΩ resistors.

The endcaps are connected to the differential amplifier via 100 pF capacitors. These capacitors let the 4 MHz ion signal pass, but block DC voltage differences between the endcaps and the amplifier.

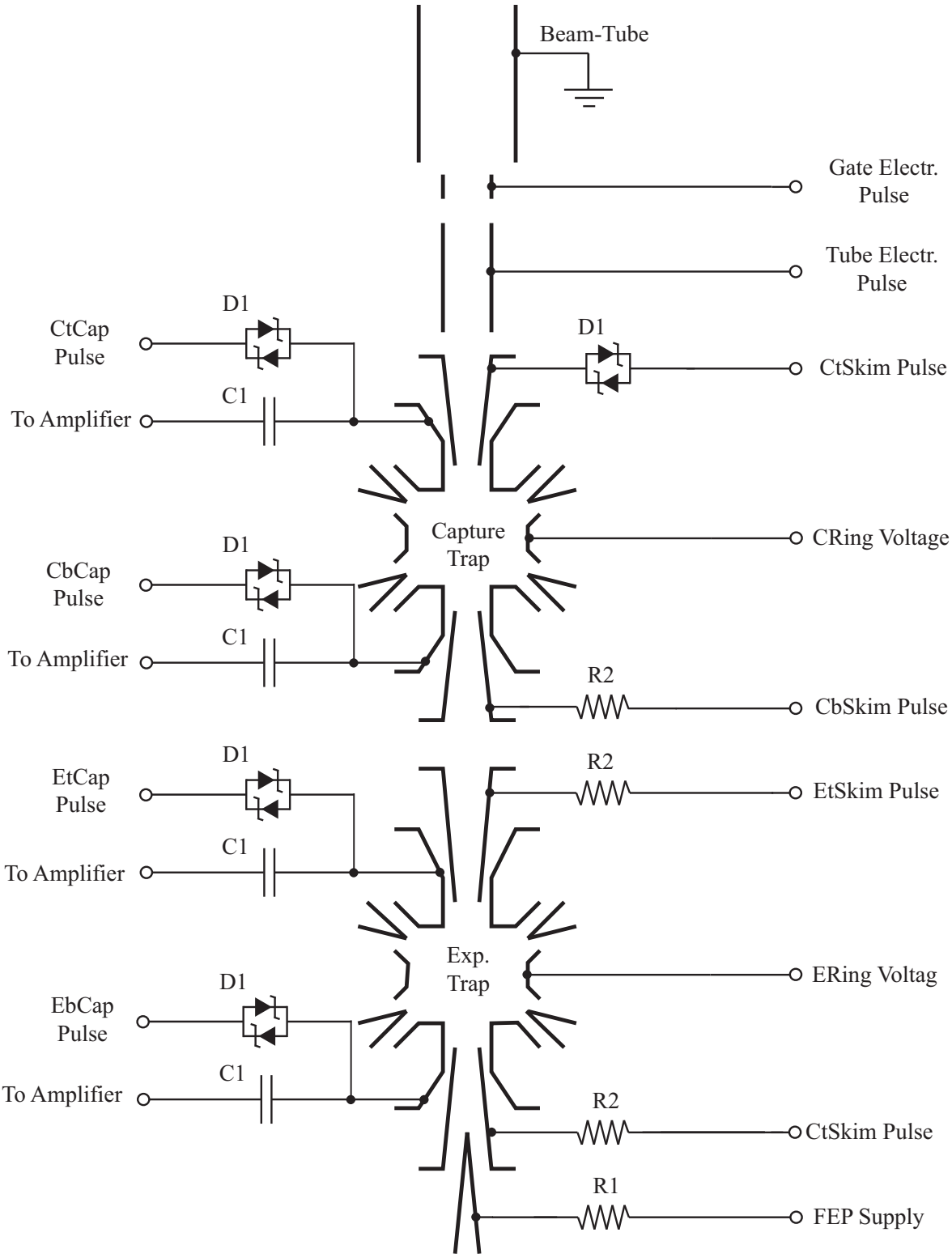

Figure 4.5: Schematic of electrode termination (guard electrode termination omitted).

Chapter 5

Commissioning Experiments

Many commissioning experiments have been performed in Heidelberg in the context of this thesis over the past year. The temperature stabilization of the magnet room has been shown to be better than 0.2 K, and the helium boil-off pressure of the superconducting magnet is controlled to a level of 0.1 pa. The vibration isolation has been confirmed to damp ground vibrations to an amplitude of less than 1 μm, and many other subsystems have been shown to work according to their specifications. The following sections focus on those commissioning experiments that are important to gauge the feasibility of the trap-to-trap transfer. These are mainly the measurements of the magnetic field (section 5.1), the trap alignment (section 5.2), and the calibration of the diode-drive-RF (section 5.3).

One of the experiment milestones in the last year was the detection of the first Heidelberg trapped-ion signal in June 2009, which is described in section 5.4.

5.1 Magnetic Field Strength

The first two attempts at charging the superconducting magnet failed and resulted in quenches due to a faulty power supply, which gave incorrect readings for the output current. In order to avoid additional magnet quenches, we applied a current of only 35.3 A to the main coil, instead of the 39 A that the magnet is specified for. Consequently, the maximum magnetic field strength is less than the 5.9 T that were used in Seattle. Because a high field NMR probe was not available at that time, the field

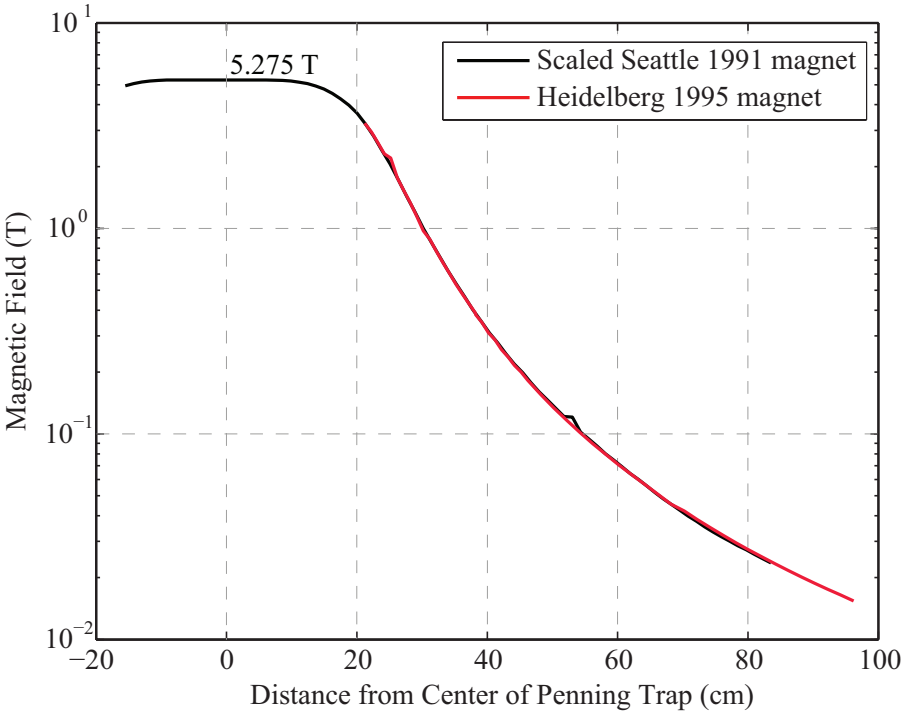

Figure 5.1: Fringe field of the superconducting magnet along z-axis. The Heidelberg measurements are shown in red. The Seattle data, shown in black, were scaled to fit the Heidelberg data, which allows an estimate of the maximum field inside the Heidelberg magnet.

strength in the center of the magnet could not be measured directly. Therefore a measurement of the fringe field along the z-axis of the magnet was taken with a hall probe, and compared to older fringe field measurements (see figure 5.1). These older measurements were performed on an identical magnet that contained the same coil setup, but was housed in a different cryostat. By scaling the older measurements to the new data, the magnetic field in the center was estimated to be (5.275 ± 0.010) T.

The field homogeneity of superconducting magnets is often expressed as a relative field deviation over a sample volume. The magnet used in this experiment is specified for a homogeneity of $10^{-8}/\mathrm{cm}^3$ at the magnet center, if the superconducting field correction coils ("shim coils") are used. Since such a homogenous magnetic field is not necessary for the recently performed test experiments, the shim coils are not used yet. As a consequence, the current homogeneity is expected to be worse by two or three orders of magnitude.

5.2 Trap Alignment

The field emission point (FEP) is not only used to create ions inside the trap, but also to check the alignment of the trap axis relative to the magnetic field, and the alignment of the electrode holes relative to each other. By biasing the FEP with −200 V and the EbSkim electrode with +100 V, an electron current of approximately 10 nA is emitted from the tip of the FEP. In the high field region, electrons with a kinetic energy of 200 eV are radially confined through their cyclotron motion, which has a radius of 8 μm or less. However, the electron beam is broadened by its own charge density to a diameter that was experimentally estimated to be about 25 μm.

If the trap is aligned perfectly with the magnetic field and all holes of the endcaps are concentric, this fine beam passes through both hyperbolic traps and the tube trap into the beamtube. By tilting the trap relative to the magnetic field, the electron beam can be made to hit certain trap electrodes, which can be measured with sensitive current meters. Knowing the geometry of the trap, we can estimate at which positions of the R1 and R2 control rods we expect the electron beam to hit the electrodes. Starting from an angle of 0° relative to the magnetic field, the beam will pass through both traps until the tilt angle reaches 0.40°, at which point the electron beam will hit the CtSkim electrode. At an angle of 0.53° the beam will start to hit CbSkim, at 0.60° it will hit EtSkim, and from 0.91° it falls on EtCap.

Figure 5.2 shows which electrodes are hit by the FEP electron beam as a function of the R1 and R2 control rod position. The experimental data agrees well with the expected values, although there are several things to consider:

1. The center of the hole has an offset relative to the center of the coordinate system. Before each lowering, the tilt-stage is adjusted such that the vacuum envelope of the traps is parallel to the beamline. This sets the center of the R1/R2 coordinate system, but can only be performed with limited accuracy. Since the offset of 4 units in each direction of the coordinate system corresponds to a misalignment of approximately 1°, there are no major problems with the trap alignment.

2. When tilting the trap to an extreme angle, i.e. more than 2.5 turns of the control rods, we observed a hysteresis phenomenon: The trap appears to return into the

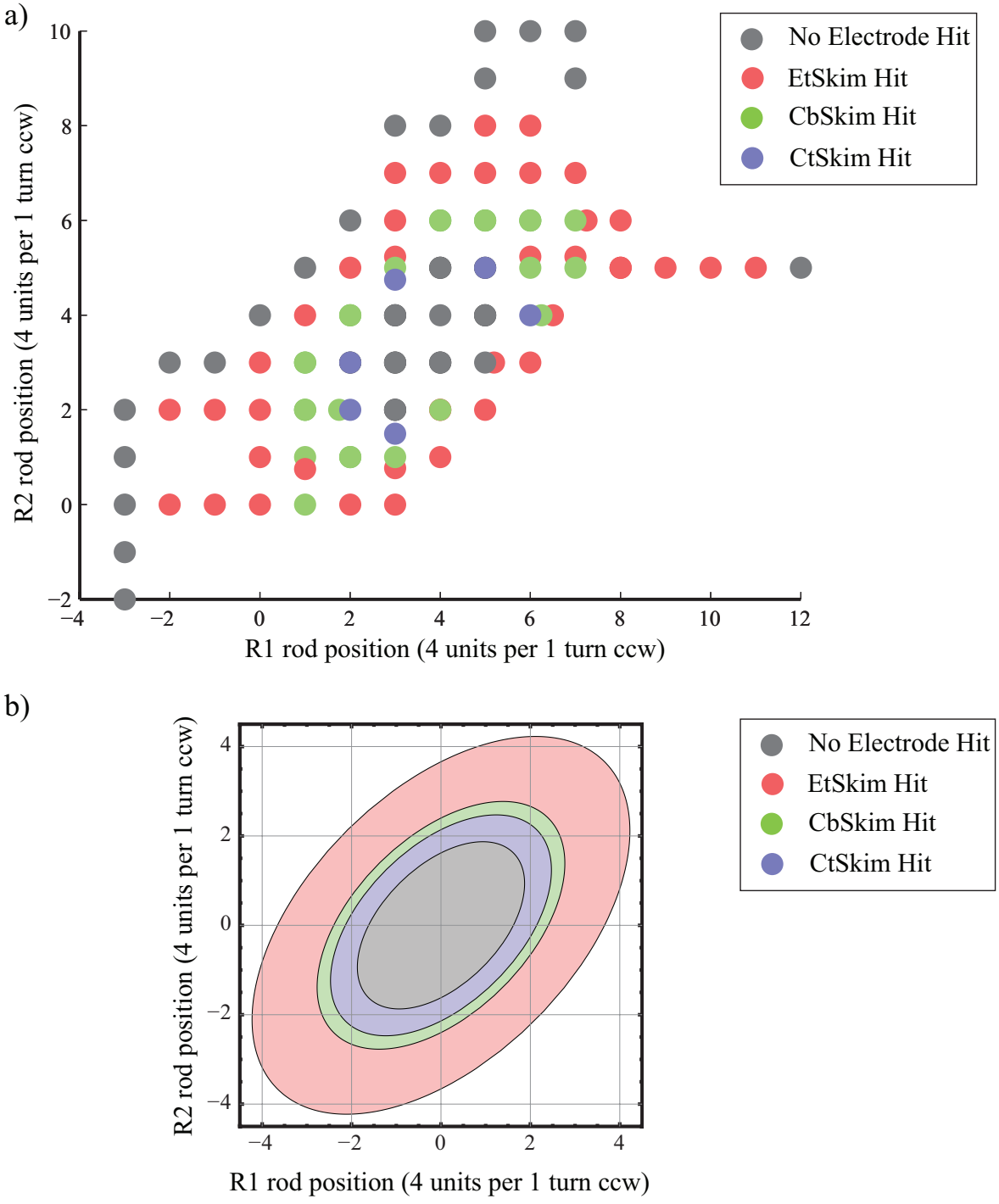

Figure 5.2: This tilt plot shows, which electrode is hit by the FEP electron beam as a function of the R1 and R2 control rod positions. The upper plot represents experimental data taken after the first successful lowering of the trap (July 2009), while the lower plot shows the expected tilt plot. The outer region of both plots corresponds to the beam hitting the EtCap electrode, which was not monitored with a current meter.

original position earlier than expected. This is due to the bore tube diameter. It limits the tilt angle to a maximum of 2.4°, which corresponds to roughly 2.5 turns of one of the control rods. When turning the control rods further, the clamps that fix the individual parts of the control rods to each other start to slip, and the trap tilt does not change any longer.

3. Due to a vacuum leak in one of the electrical feedthroughs, the beamline had to be pulled out of the magnet, and the trap vacuum had to be broken. After lowering the beamline into the magnet again, the electron beam could not passed reliably through the EtSkim electrode. It is possible that, as the traps were exposed to air, a foreign particle entered the inside of the EtSkim electrode and is partially blocking its hole. Further tests to prove this assumption are presently ongoing and steps to solve the problem taken.

Despite these issues, it was shown that the holes inside the electrode are concentric, and that this method can in principle be used to align the trap axis with the magnetic field. However, the blocking problem may necessitate the disassembly of the traps before a trap-to-trap transfer can be attempted.

5.3 Diode-Drive-RF Calibration

Figure 5.3 shows the potential of the CtCap electrode during a pulse for various amplitudes of the diode-drive-RF. The pulse shown corresponds to a tube-to-trap transfer sequence and is very similar to a trap-to-trap pulse, only shorter. A diode-drive-RF amplitude of $1.6\mathrm{V_{pp}}$ seems to optimize the pulse shape. However, in the first 0.4 μs after each pulse edge, the pulse height deviates by up to 200 mV from the ideal shape due to some remaining excitation of the LC circuit. This deviation is very reproducible from pulse to pulse. Further, the diode-drive-RF blurs the pulse height by coupling onto the electrode with an amplitude of $70\,\mathrm{mV}_{pp}$. For the tube-to-trap transfer, such deviations are acceptable, because the high number of ions inside the tube trap permits a certain level of ion loss. The impact of the pulse deviations on the trap-to-trap transfer will be discussed in chapter 6.

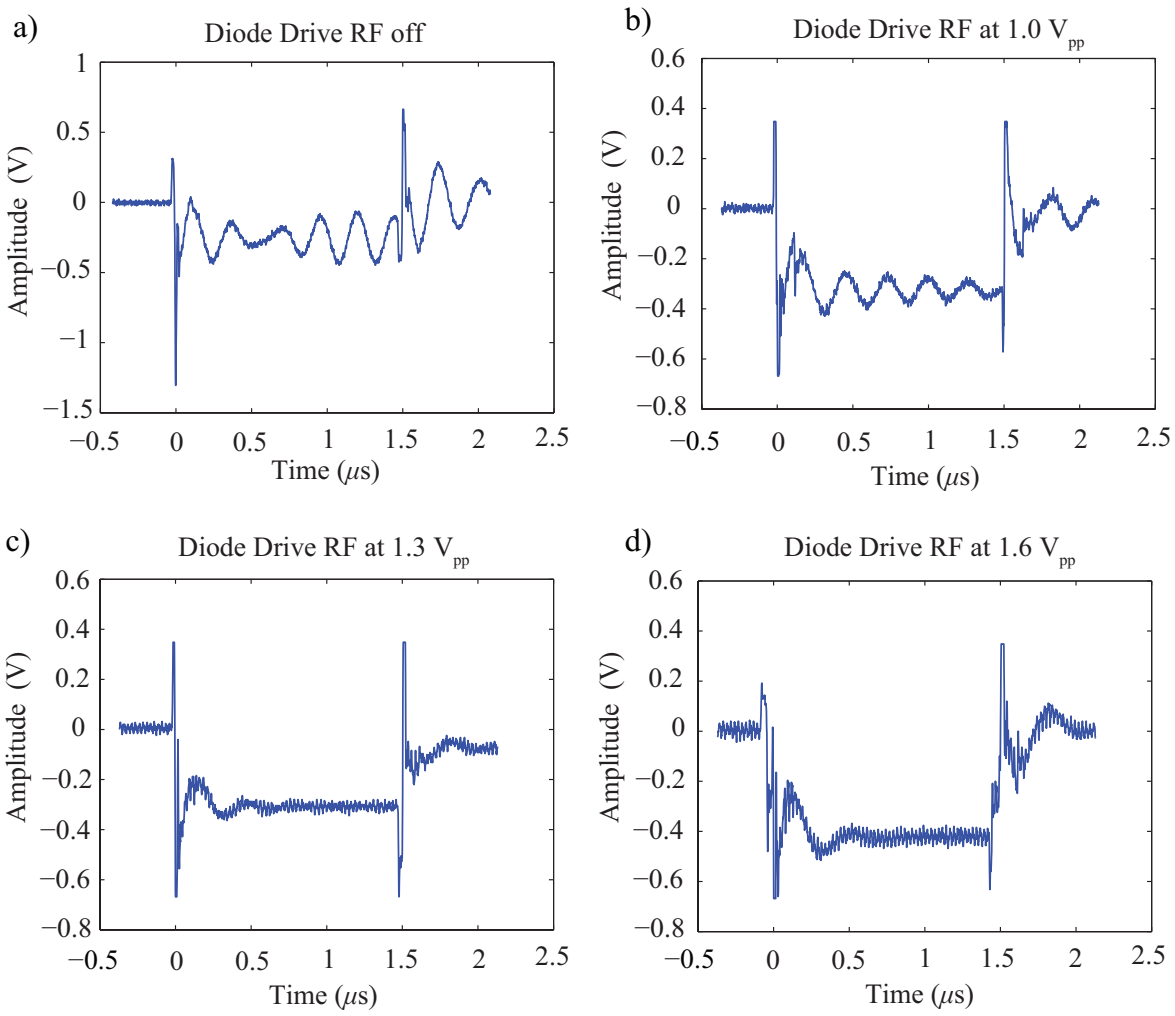

Figure 5.3: Voltage on CtCap electrode during Tube-To-Trap transfer for various amplitudes of the diode-drive-RF. If the diode-drive-RF is off, the 4 MHz ringing of the LC circuit is clearly visible, and the overall pulse is less deep than $V_{\text{transfer}} = -0.5\,\text{V}$ (figure a). As the diode-drive-RF amplitude is turned up, the 4 MHz ringing goes down and the pulse depth approaches V_{transfer} (figure b and c). For an optimal diode-drive-RF amplitude of $1.60\,\text{V}_{\text{pp}}$, the pulse is $-0.5\,\text{V}$ deep, but some ringing continues to be present (figure d). Increasing the amplitude further does not reduce the ringing, but increases the coupling of the diode-drive-RF signal onto the electrode. The influence of the ringing on the trap-to-trap sequences will be discussed in chapter 6.

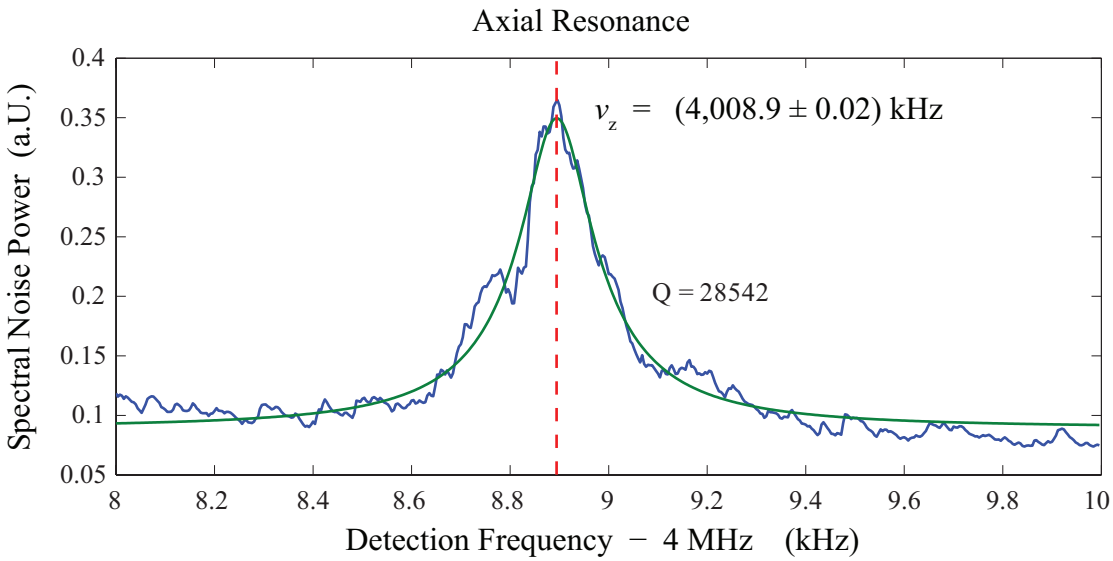

Figure 5.4: Plot of the axial frequency resonance of several thousand $^{12}C^{4+}$ ions in the noise spectrum of the amplifier, taken directly after loading. The blue line represents the data while the green line is a Lorentzian fit yielding a quality factor of 28542.

5.4 First Ion Signals

Before the setup of the external ion source was completed, the experiment trap was loaded by ionizing rest gas inside the trap with the field emission point. The first Heidelberg ion signal ($^{12}C^{4+}$) was observed on June 6th, 2009. Since $^{12}C^{4+}$ ions have the same charge to mass ratio as $^{3}H^{+}$ and $^{3}He^{+}$, they were used to characterize the experiment trap. Figure 5.4 shows an axial frequency scan for an ion cloud of several thousand $^{12}C^{4+}$ ions. This plot was taken by observing the noise power spectrum of the amplifier output shortly after loading the trap with the field emission point. The hot ions cool down by dissipating their energy into the tuned LC circuit. They are visible in the noise spectrum as a Lorentzian shape with a quality factor $Q_{\text{ions}} \approx 20,000$ that is much higher than the quality factor $Q_{\text{LC}} \approx 1000$ of the LC circuit.

A magnetron resonance can be seen in figure 5.5. For such a measurement the axial frequency is locked at 4 MHz by closing the ring voltage feedback loop. The "magnetron cooling drive" signal is applied and swept upwards in frequency, until it coincides with the cooling resonance of the ion. As the energy in the magnetron mode is changed, the axial frequency of the ion is slightly modified due to higher order effects in the electric and magnetic fields. This frequency change is measured by the detection circuit, and

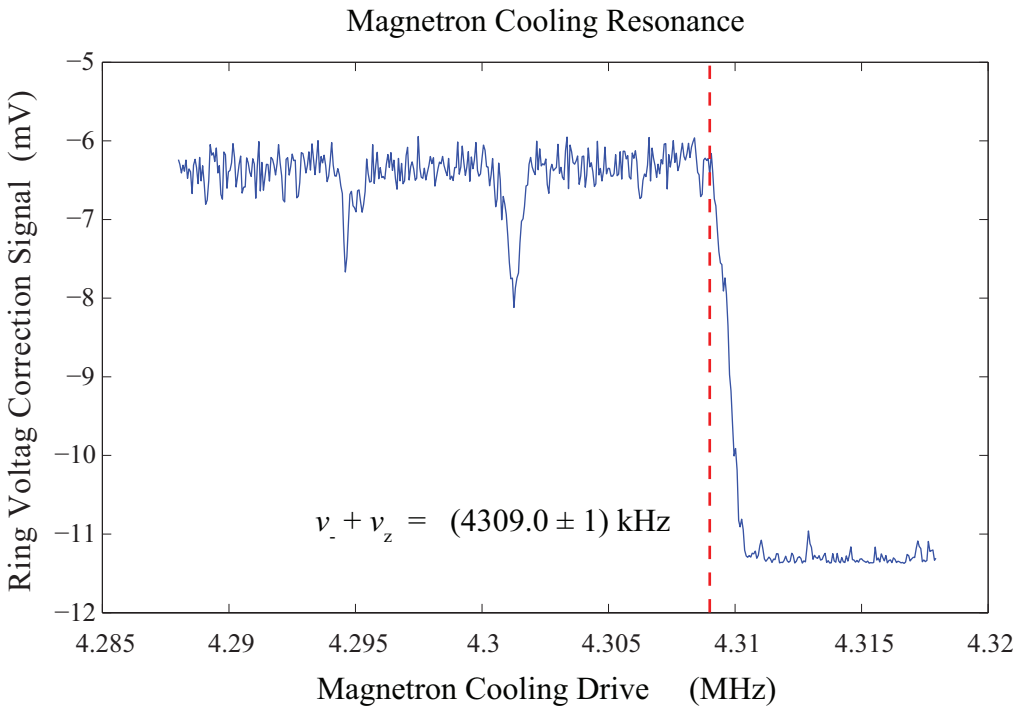

Figure 5.5: Plot of the magnetron cooling resonance of several hundred ions. The spikes at 4.295 MHz and 4.301 MHz are due to short disruptions of the detection circuit, which causes the locked loop to lose stability for a fraction of a second.

is expressed in the ring voltage correction signal.

The reduced cyclotron frequency ν_+ is measured through direct, dipolar excitation (figure 5.6). The feedback loop is closed and a dipolar RF signal is applied and swept upwards in frequency. The energy change in the cyclotron mode modifies the axial frequency, which influences the ring voltage correction signal.

Since the charge to mass ratio of $^{12}C^{4+}$ is known to a high precision, the magnetic field strength at the center of the experiment trap can be calculated, which yields: $B = (5.259 \pm 0.001)\,\mathrm{T}$. This is in good agreement with the value $B = (5.275 \pm 0.010)\,\mathrm{T}$ obtained through the Hall probe measurements of the magnetic fringe field.

In a recent development a μA electron beam from the ion source was used to ionize rest gas inside the capture trap, which marked the first loading of this trap. Current work is ongoing to characterize the capture trap, and to use the electron beam from the ion source for further trap alignment studies.

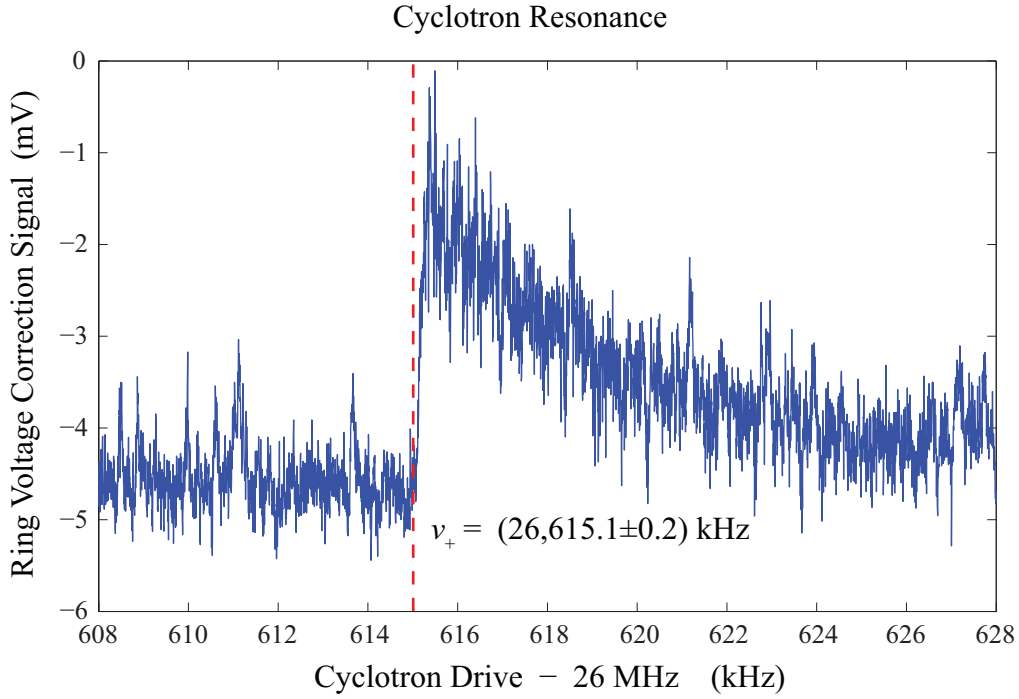

Figure 5.6: Plot of the cyclotron resonance of several hundred ions. The cyclotron drive signal was changed with a sweep-rate of 200 Hz/s. The observed relaxation of the ring voltage correction signal corresponds to a relaxation time of 25 s, which is due to collisional damping of the cyclotron energy in the ion cloud.

Chapter 6

Discussion

Equipped with the results of the commissioning experiments, the feasibility of the trap-to-trap transfer scheme can be examined in detail. After a discussion of the initial state of the ion transfer in section 6.1, the radial and axial electric fields during the transfer are investigated in section 6.2. Section 6.3 motivates that the equations of motion can be seperated into an axial and radial mode. The influence of axial perturbations to the ideal pulse shape, for instance due to the diode-drive-RF and the ringing of the LC circtuit, will be treated in section 6.4, while the influence of radial electric fields will be discussed in section 6.5.

The focus will be on ions with a charge of 1 e and a mass of 3 u, but the results can easily be generalized to ions with a different charge-to-mass ratio.

6.1 Initial State of the Ion Transfer

Each transfer attempt begins by cooling the cyclotron and magnetron modes of the ion, in order to prepare a reproducible and well localized initial state. The cooling is most effective, if the ion can dissipate its energy into the LC detection circuit. The axial frequency must therefore be at 4 MHz, which necessitates a ring voltage V_0 of approximately -87 V. After cooling, the ion is in a state where it can be described by the values given in table 2.2. The ring voltage is then gradually reduced to $V_{0\mathrm{t}} = -0.5\,\mathrm{V}$, which sets the initial state for the ion transfer. The time constant for this potential reduction is of the order of 1 ms, which is much larger than any of the ion motion

Table 6.1: Calculated energies and motion radii for the initial state of the ion transfer. The top row corresponds to an ion state after a cooling with quadrupolar RF signals at a ring voltage of $-87\,\mathrm{V}$, while the bottom row gives the ion state after reducing the ring voltage adiabatically to $-0.5\,\mathrm{V}$.

V_0	E_z	ρ_z	E_+	ρ_+	E_-	ρ_-
$-87\,\mathrm{V}$	$3.8 \times 10^{-4}\,\mathrm{eV}$	$9.3\,\mu\mathrm{m}$	$5.8 \times 10^{-3}\,\mathrm{eV}$	$3.6\,\mu\mathrm{m}$	$6.5 \times 10^{-7}\,\mathrm{eV}$	$3.6\,\mu\mathrm{m}$
$-0.5\,\mathrm{V}$	$2.9 \times 10^{-5}\,\mathrm{eV}$	$2.6\,\mu\mathrm{m}$	$5.8 \times 10^{-3}\,\mathrm{eV}$	$3.6\,\mu\mathrm{m}$	$3.7 \times 10^{-9}\,\mathrm{eV}$	$3.6\,\mu\mathrm{m}$

periods, i.e. it can be seen as an adiabtic change. This allows an estimate of the properties of the initial state by using the adiabatic invariants (see section 2.2.1).

The adiabatic invariant of the axial mode I_z constrains the ratio $\frac{E_z}{\omega_z}$. With the equations (2.11) and (2.20) this adiabatic invariant can be stated as:

$$E_z \propto {V_0}^{1/2} \tag{6.1}$$

$$\rho_z \propto {E_z}^{1/2} \propto {V_0}^{1/4} \quad . \tag{6.2}$$

In the reduced cyclotron mode, the adiabatic invariant sets a relationship between the cyclotron radius ρ_+ and the reduced cyclotron frequency ω_+. Since the latter does not change significantly with the ring voltage, the radius and energy in this mode stay approximately constant.

The adiabatic invariant of the magnetron mode is proportional to the magnetic flux through the area enclosed by the magnetron motion. Since the magnetic field is unchanged by the reduction of the ring voltage, the magnetron radius stays constant. The energy in the magnetron mode mainly consists of potential energy (the kinetic energy at the low speed of the magnetron motion is negligible). Since the potential energy at a constant radius is directly proportional to the ring voltage, E_- is linearly reduced with the ring voltage.

With these proportionalities and the values from table 2.2, the initial state of the ion can be calculated. The results are given in table 6.1.

6.2 Electric and Magnetic Fields

Before the equations of motion can be solved, the electric and magnetic fields inside the trap must be addressed. During the pulse, one of the endcaps is biased with V_{transfer}. In order to estimate the resulting axial and radial electric fields, the simulation program SIMION 8 [33] was used to numerically solve the corresponding boundary condition problem. The simulated potential along the z-axis is shown in figure 6.1. Since the output of the simulation program consists of discrete values for the potential (spatial resolution: $40\,\mu$m), a cubic polynomial was fitted to the simulation data:

$$\Phi(0,z) = -4.792 \times 10^6 \frac{\text{V}}{\text{m}^3} z^3 + 2.868 \times 10^4 \frac{\text{V}}{\text{m}^2} z^2 - 88.1 \frac{\text{V}}{\text{m}} z - 0.3914\,\text{V} \tag{6.3}$$

The radial electric field was also fitted with a polynomial. As can be seen in figure 6.2, a quadratic function suffices to describe the radial potential:

$$\Phi(\rho,0) = 1.455 \times 10^4 \frac{\text{V}}{\text{m}^2} \rho^2 - 0.3914\,\text{V} \tag{6.4}$$

For symmetry reasons, all odd order terms have to be zero.

Both fit-functions agree in the way that they give the same potential for the trap center $(\rho, z) = (0, 0)$. Their derivatives can be used to evaluate the electric fields at the beginning of the ion transfer. At a radial displacement of the order of $\rho_+ + \rho_-$, the radial electric field E_ρ is of the order of $0.2\,\text{V/m}$, while the initial axial electric field amounts to approximately $88\,\text{V/m}$.

Another electric field of interest is the field between the endcaps and the adjacent skimmer electrodes. It is the strongest electric field in this transfer, since a voltage drop of $3.5\,\text{V}$ occurs over a distance of only $0.89\,\text{mm}$. Due to symmetry reasons, the radial components of this field must be negligible near the trap axis, and due to the short length of the field, the ion passes it in a time of about $100\,\text{ns}$, which keeps influences of the exact field shape small. For initial calculations, it is assumed to be homogeneous and purely in the axial direction.

Ideally, the electric field inside the skimmer electrodes is zero. However, surface charge and patch potentials can potentially create radial electric fields. Their influence will be investigated in section 6.5.

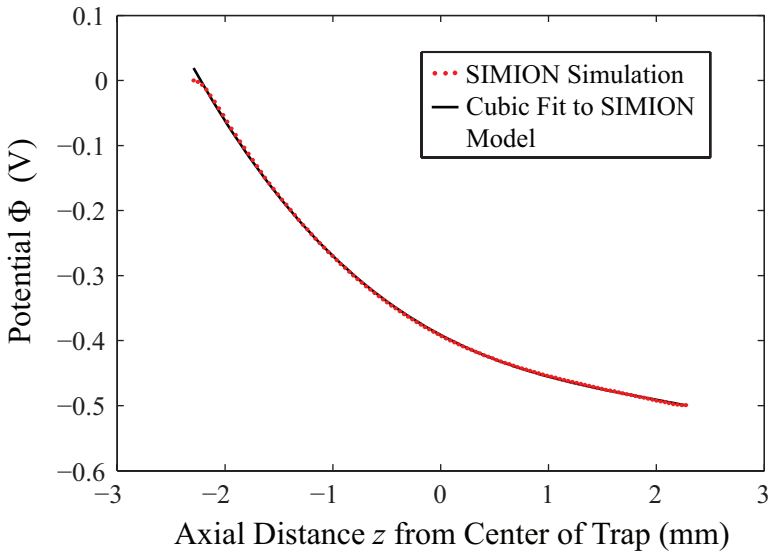

Figure 6.1: Axial potential inside the hyperbolic traps during a trap-to-trap transfer. The potential field was calculated using SIMION 8 (red dots), and then fitted with a cubic polynomial (black line).

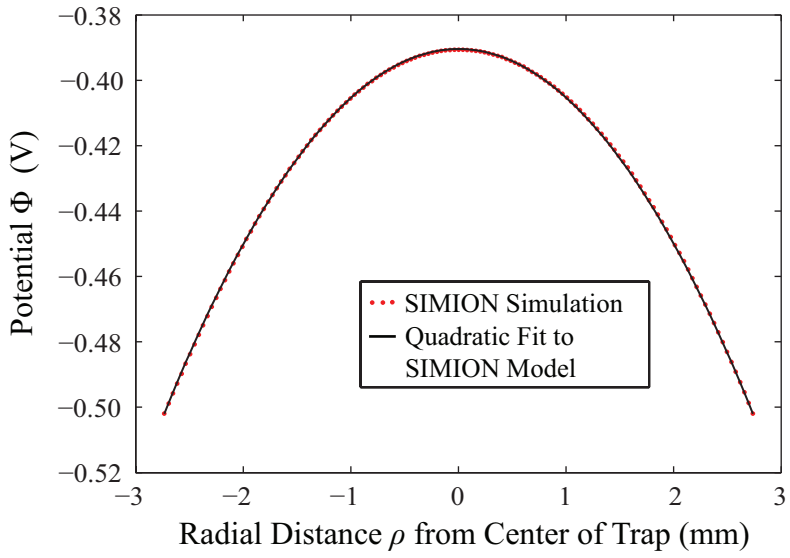

Figure 6.2: Radial potential inside the hyperbolic traps during a trap-to-trap transfer. The potential is shown along a radial line that intersects the trap center.

6.3 Equations of Motion

In order to be able to use the guiding center motion as described in section 2.2.2, the length scale of the field variations has to be small compared to the cyclotron radius. Technically this is not true in the case of a well focused ion in the beginning of the transfer. Since in the cooling limit the cyclotron radius equals the magnetron radius, the cyclotron motion will sample electric fields with *relatively* large variations. However, speaking in *absolute* terms, the field variations are small. Further, the axial field, which is stronger by three orders of magnitude during the beginning of the transfer, quickly extracts the ion out of the endcap into the skimmer electrodes, where, in the ideal case, the radial electric fields are zero.

Therefore, an application of the guiding center technique is valid, but due to the field variations being on the same scale as the magnetron radius, the application of the $\vec{E} \times \vec{B}$ drift can only give an order of magnitude estimation on possible drift velocities.

Equation (2.25) contains a term that is proportional to the gradient of the absolute magnetic field strength. The magnetic field was not optimized after charging, and the capture trap is approximately 4 cm away from the most homogeneous field region, which implies that the magnetic field homogeneity over the transfer distance must be assumed to be much worse than the $10^{-8}\,\mathrm{T/cm^3}$ that the magnet is specified for. But due to the very small magnetic moment $\mu_c = \frac{1}{2} q \omega_+ \rho_+^2 = 1.8 \times 10^{-22}\,\mathrm{J/T}$ of the cooled cyclotron motion, the coupling of the ion motion to the magnetic field inhomogeneities is very weak compared to the electric forces. Even for field gradients as big as $10^{-4}\,\mathrm{T/m}$, the resulting force on the ion is three orders of magnitude smaller than the force due to the axial and radial electric fields at the beginning of the transfer. The gradient of the magnetic field can therefore be neglected.

This allows us to use the guiding center motion in its simplest form: A one dimensional differential equation for the axial direction:

$$\ddot{\vec{z}} = \frac{q}{m} \vec{E}_z(z) \quad , \tag{6.5}$$

and an $\vec{E} \times \vec{B}$-drift in the radial plane:

$$\vec{v}_{\mathrm{drift}} = \frac{\vec{E} \times \vec{B}}{B^2} \quad . \tag{6.6}$$

Table 6.2: Ion transfer time for a transfer from the experiment trap to the capture trap, broken down into individual sections.

time	value	description
t_1	$1.43\,\mu$s	From center of experiment trap to EtCap
t_2	$0.19\,\mu$s	Inside EtCap hole
t_3	$0.11\,\mu$s	Between EtCap and EtSkim
t_4	$2.40\,\mu$s	Inside EtSkim and CbSkim
t_5	$0.11\,\mu$s	Between CbSkim and CbCap
t_6	$0.19\,\mu$s	Inside CbCap hole
t_7	$1.43\,\mu$s	From CbCap to center of capture trap
t_t	$5.83\,\mu$s	Total transfer time

However, as stated above, it has to be kept in mind that the relative error of the $\vec{E} \times \vec{B}$-drift might become considerably big.

6.4 Ion Loss in the Axial Mode

The simulation of the electric field inside the traps, and the assumptions about the electric field between the traps can be used to integrate the initial value problem posed by equation (6.5). This integration was performed piecewise using the computer program Mathematica [34] and is summarized in table 6.2. The ion loss was parameterized by examining the ion energy $E_{\text{end}} = E_{\text{kin}} + E_{\text{pot}}$ at the end of the transfer. An optimal transfer pulse does not change the energy in the axial mode. In this case, the kinetic energy of the ion would be negligible, and the potential energy would correspond to the well depth of the Penning trap, i.e. $E_{\text{end}} = -0.293\,\text{eV}$ for a ring voltage of $-0.5\,\text{V}$. In a non-ideal case, the pulse would cause the end energy to be higher. For $E_{\text{end}} \geq 0$, the ion cannot be trapped anymore and is lost. Figure 6.3 shows, how a non-optimal pulse length changes the end energy of the ion. This plot can be used to illustrate the influence of the 50 ns resolution of the pulse timing electronics. By setting the pulse length at $5.85\,\mu$s, which is only 20 ns from the optimum pulse length of $5.85\,\mu$s, the end energy changes by less than $10^{-4}\,\text{eV}$. Other effects that can transfer energy into

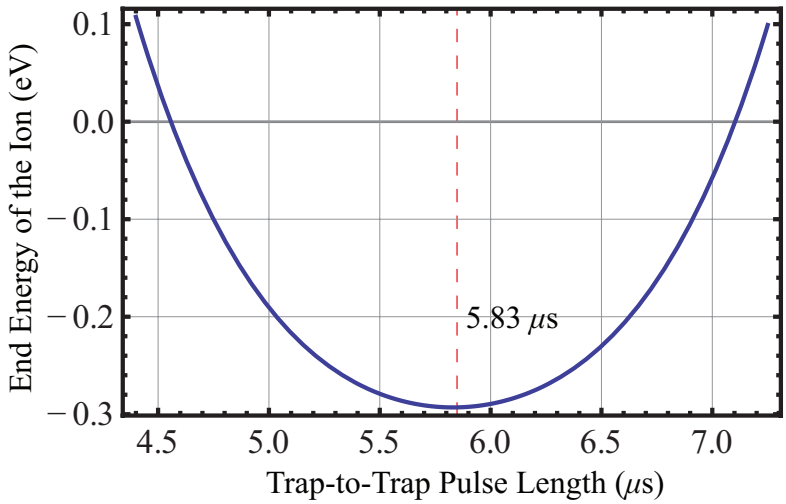

Figure 6.3: Energy of the ion at the end of a trap-to-trap sequence. For this plot, the pulse shape was assumed to be ideal, and the pulse length was varied. At the optimal pulse length of 5.83 μs, the energy of the ion is equal to the potential energy inside the trap center. As the pulse length is varied, the ion will have a higher potential and a higher kinetic energy at the end of the transfer. For $E_{\text{end}} \geq 0$, the ion is lost.

the axial ion motion are:

- Initial phase of the axial motion: Before the transfer, the ion performs a harmonic oscillation in the axial mode with an energy that is given by table 6.1. At the beginning of the pulse, the initial velocity can point either towards or away from the transfer direction. However, because of the small energy in the adiabatically cooled axial mode, the initial velocity is small and the overall effect negligible. In the case of an ideal rectangular pulse shape, the transferred energy is less than 10^{-4} eV.

- Ringing of the LC circuit. The pulse height during the first 0.4 μs deviates from the ideal pulse height by approximately 100 mV. This leads to an acceleration of the ion with a time-varying electric field. But, since the ion is essentially at rest in the beginning of the transfer, the total effect of the pulse deviation is small. A numerical integration with a time varying electric field strength resulted in a t_1-change of the order of 1 ns and an energy transfer below 10^{-4} eV.

- Diode-Drive-RF influence. The 40 MHz diode-drive-RF couples with an amplitude of 70 mV_{pp} onto the endcap electrodes, which influences the electric field

between the endcaps and skimmer electrodes. Since this amplitude is small compared to the 3.5 V voltage drop, the effect of the diode-drive-RF is expected to be small. A quantitative estimation yielded an energy transfer on the level of 10^{-3} eV.

These results indicate that even though the electrode pulses deviate considerably from the ideal shape, ion loss in the axial mode does not constitute a problem.

6.5 Ion Loss in the Radial Mode

Ion loss in the radial mode occurs if the ion drifts further away from the trap axis than the 125 μm radius of the EtSkim electrode hole. Initially, the ion has a radial displacement of less than 10 μm (see table 6.1).

In the ideal case, the electric fields in the radial plane are only caused by the trap geometry. Since the trap is rotationally symmetric, the radial electric fields can be approximated with a quadrupolar field. This leads to a magnetron type motion around the trap axis. At the start of the ion transfer, the electric field given by equation (6.4) would lead to a magnetron type motion with a frequency of approximately 1 kHz. Since the ion transfer lasts less than 6 μs, this motion can be ignored.

However, patch potentials break the trap symmetry. These potentials arise from different values of the work function across the surface of the electrodes, and from surface contaminants. They cause a change of potential along the electrode's area, which is between 1 mV for gold surfaces to 70 mV for phosphor bronze surfaces. The dimension of these patches is typically in the range of 10 μm, but patches in the length scale of several mm have been found for phosphor bronze electrodes [35].

The skimmer electrodes are made of oxygen-free high conductivity (OFHC) copper and are not gold plated. The patch potential strength should therefore be assumed to be in the order of 10 mV. In the worst case, a large patch potential leads to an electric field that points in a constant direction over the course of the ion transfer. This would cause an $\vec{E} \times \vec{B}$ drift that radially displaces the ion. For estimating the order of magnitude of this effect, a crude model can be used: The electric field due to a 10 mV patch potential inside a tube such as a skimmer electrode with a mean diameter

of 1 mm will be about 10 V/m. Inside the 5 T B-field this causes an $\vec{E} \times \vec{B}$-drift velocity of 2 m/s. The ion will drift in the radial plane with this velocity for the time it is inside the skimmer electrodes. This time is given by table 6.2, and is in the order of 3 μs, which leads to a radial displacement of 6 μm. Consequently, under the influence of large patch potentials, no ion loss should occur in the radial mode for the pulse times shown in table 6.2. This holds true even for an additional radial displacement caused by a misalignment of the electrode holes, which is expected to be of the order of 10 μm (see figure 5.2).

However, the guiding center motion may not always be a suitable approach to the calculation of the axial displacement. The size of the patch potentials is unlikely to be in the order of mm. For smaller patches, the radial electric fields change on a timescale of the cyclotron motion as the ion moves through the skimmer electrodes, which can transfer energy in or out of the cyclotron motion. For a more stringent analysis, it may be necessary in the future to perform a numerical simulation of the ion flight, using realistic patch potential distributions and a numerical evaluation of the field between the endcaps and skimmer electrodes.

6.6 Summary

It was shown that the ion loss in the axial mode does not constitute a problem. The influence of the non-ideal electrode pulses is negligible, which allows us to even shorten the transfer time by using stronger voltage pulses. A shorter transfer time would mitigate problems that arise from patch potentials, as the interaction time with the patches decreases with the ion's velocity. On the other hand, an increase in the pulse depth also increase the radial electrical fields caused by the trap geometry.

The optimal pulse bias voltages could be investigated through further, detailed simulations. On the other hand, since there are only three parameters to this optimization problem (V_{transfer}, V_{drift}, and the pulse length), and since the simulations that were performed so far make us confident that the transfer scheme will work, the next step will be to verify the trap-to-trap transfer experimentally.

Chapter 7

Conclusion and Outlook

Over the course of the last year, the relocation of the UW/MPIK-PTMS from Seattle to Heidelberg was completed. The new laboratory, which was specifically designed and constructed to meet the requirements of this experiment, has been equipped with environmental control systems that stabilize, besides the magnetic field, the room temperature and the magnet cryostat boil-off pressure. The superconducting magnet has been energized, and the setup of the ion detection electronics was completed, which led to the detection of the first Heidelberg trapped-ion signal within this thesis work. The external ion source has been recently commissioned and can now be used to send a beam of either electrons or ions into the capture trap. Both traps can be reliably loaded through *in situ* rest gas ionization with electron beams from the field emission point or the ion source, clearly demonstrating the success of the trap alignment procedure described in chapter 5.

In the work presented here it was shown in addition that the ambitious trap-to-trap transfer scheme, which is designed to transfer single ions between the two Penning traps, is not restricted by the considerable variations of the transfer voltage pulses. The misalignment of the small holes that the ions have to pass was also shown to be well within tolerable limits. A possible limitation of the ion transfer may arise due to radial electric fields caused by patch potentials, but in first estimations the impact of these potentials on the radial displacement of the ion was small. However, a better model is needed to quantitatively estimate their influence.

After the successful storage and detection of a cloud of protons and $^{12}C^{4+}$ ions

in the trap, a particle reduction and single ion detection sensitivity has still to be demonstrated before a first mass measurement can be performed.

Bibliography

[1] K. Blaum. High-accuracy mass spectrometry with stored ions. *Physics Reports*, 425(1):1–78, 2006.

[2] K. Blaum, G. Audi, D. Beck, G. Bollen, F. Herfurth, A. Kellerbauer, H.-J. Kluge, E. Sauvan, and S. Schwarz. Masses of ^{32}Ar and ^{33}Ar for fundamental tests. *Phys. Rev. Lett.*, 91(26):260801, 2003.

[3] R. S. Van Dyck, Jr., S. L. Zafonte, and P. B. Schwinberg. Ultra-precise mass measurements using the UW-PTMS. *Hyperfine Interactions*, 132(1–4):163–175, 2001.

[4] S. Rainville, J. K. Thompson, and D. E. Pritchard. An Ion Balance for Ultra-High-Precision Atomic Mass Measurements. *Science*, 303(5656):334–338, 2004.

[5] R. S. Van Dyck, Jr., D. L. Farnham, and P. B. Schwinberg. Tritium–helium-3 mass difference using the Penning trap mass spectroscopy. *Phys. Rev. Lett.*, 70(19):2888–2891, 1993.

[6] Ø. Elgarøy and O. Lahav. Neutrino masses from cosmological probes. *New Journal of Physics*, 7:61, 2005.

[7] Y. Fukuda, T. Hayakawa, E. Ichihara, K. Inoue, K. Ishihara, H. Ishino, Y. Itow, T. Kajita, J. Kameda, S. Kasuga, K. Kobayashi, Y. Kobayashi, Y. Koshio, M. Miura, M. Nakahata, S. Nakayama, A. Okada, K. Okumura, N. Sakurai, M. Shiozawa, Y. Suzuki, Y. Takeuchi, Y. Totsuka, S. Yamada, M. Earl, A. Habig, and E. Kearns. Evidence for oscillation of atmospheric neutrinos. *Phys. Rev. Lett.*, 81(8):1562–1567, 1998.

[8] J. Kraus, Ch. Bonn, B. Bornschein, L. Bornschein, B. Flatt, A. Kovalik, B. Muller, E. W. Otten, J. P. Schall, T. Thummler, and Ch. Weinheimer. Latest results from the Mainz neutrino mass experiment. *Nuclear Physics A*, A721:533c–6c, 2003.

[9] E. W. Otten and C. Weinheimer. Neutrino mass limit from tritium β-decay. *Reports on Progress in Physics*, 71(8):086201–, 2008.

[10] Sz. Nagy, T. Fritioff, M. Björkhage, I. Bergström, and R. Schuch. On the Q-value of the tritium β-decay. *Europhys. Lett.*, 74:404–410, 2006.

[11] F. M. Penning. Die Glimmentladung bei niedrigem Druck zwischen koaxialen Zylindern in einem axialen Magnetfeld. *Physica*, 3:873–894, 1936.

[12] J. R. Pierce. *Theory and Design of Electron Beams*. D. Van Nostrand Co., New York, 1949.

[13] R. S. Van Dyck, Jr., P. B. Schwinberg, and H. G. Dehmelt. New high-precision comparison of electron and positron g-factors. *Phys. Rev. Lett.*, 59(1):26–29, 1987.

[14] R. S. Van Dyck, Jr., F. L. Moore, D. L. Farnham, and P. B. Schwinberg. New measurement of the proton-electron mass ratio. *International Journal of Mass Spectrometry and Ion Processes*, 66:327–337, 1985.

[15] D. L. Farnham. *A determination of the proton/electron mass ratio and the electron's atomic mass via Penning trap mass spectroscopy*. PhD thesis, University of Washington, Seattle, 1995.

[16] F. Rossi and G. I. Opat. Observations of the effects of adsorbates on patch potentials. *Journal of Physics D: Applied Physics*, 25(9):1349–1353, 1992.

[17] V. Natarajan. *Penning Trap Mass Spectroscopy at 0.1 ppb*. PhD thesis, MIT, 1993.

[18] M. Redshaw. *Precise Measurements of the Atomic Masses of ^{28}Si, ^{31}P, ^{32}S, ^{84,86}Kr, ^{129,132,136}Xe, and the Dipole Moment of PH^+ using Single-Ion and Two-Ion Penning Trap Techniques*. PhD thesis, Florida State University, 2007.

[19] L. S. Brown and G. Gabrielse. Geonium theory: Physics of a single electron or ion in a Penning trap. *Rev. Mod. Phys.*, 58(1):233–311, 1986.

[20] G. Gabrielse. Why is sideband mass spectrometry possible with ions in a Penning trap? *Phys. Rev. Lett.*, 102(17):172501, 2009.

[21] D. B. Pinegar. *Tools for a precise tritium to helium-3 mass comparison.* PhD thesis, University of Washington, Seattle, 2007.

[22] J. K. Thompson. *Two-ion control and polarization forces for precise mass comparisons.* PhD thesis, Massachusetts Institute of Technology, Cambridge, MA, Sept. 2003.

[23] L. D. Landau and E. M. Lifshitz. *Course of Theoretical Physics 1.* Butterworth Heinemann, 1976.

[24] M. Kretzschmar. Single particle motion in a Penning trap: description in the classical canonical formalism. *Physica Scripta*, 46(6):544–554, 1992.

[25] J. Notte, J. Fajans, R. Chu, and J. S. Wurtele. Experimental breaking of an adiabatic invariant. *Phys. Rev. Lett.*, 70(25):3900–3903, 1993.

[26] Theodore G. Northrop. *The Adiabatic Motion of Charged Particles.* Interscience Tracts on Physics and Astronomy, 1963.

[27] R. S. Van Dyck, Jr., D. L. Farnham, S. L. Zafonte, and P. B. Schwinberg. Ultrastable superconducting magnet system for a Penning trap mass spectrometer. *Rev. Sci. Instruments*, 70(3):1665–1671, 1999.

[28] D. B. Pinegar, K. Blaum, T. P. Biesiadzinski, S. L. Zafonte, and R. S. Van Dyck, Jr. Stable voltage source for Penning trap experiments. *Review of Scientific Instruments*, 80(6):064701, 2009.

[29] B. F. Gavin. PIG ion sources. In I. G. Brown, editor, *The Physics and Technology of Ion Sources*, page 167. Whiley, New York, 1989.

[30] E. W. McDaniel. *Collision phenomena in ionized gasses.* Wiley, New York, 1964.

[31] H. G. Dehmelt and F. L. Walls. "Bolometric" technique for the RF spectroscopy of stored ions. *Phys. Rev. Lett.*, 21(3):127–131, Jul 1968.

[32] MCE Metelics Corporation. MGS902 Datasheet. Sunnyville, CA, 2003.

[33] David A. Dahl. SIMION for the personal computer in reflection. *International Journal of Mass Spectrometry*, 200(1-3):3 – 25, 2000.

[34] *Mathematica Edition Version 7.0.* Wolfram Research, Inc., Champaign, IL, 2008.

[35] J. B. Camp, T. W. Darling, and Ronald E. Brown. Macroscopic variations of surface potentials of conductors. *Journal of Applied Physics*, 69(10):7126–7129, 1991.